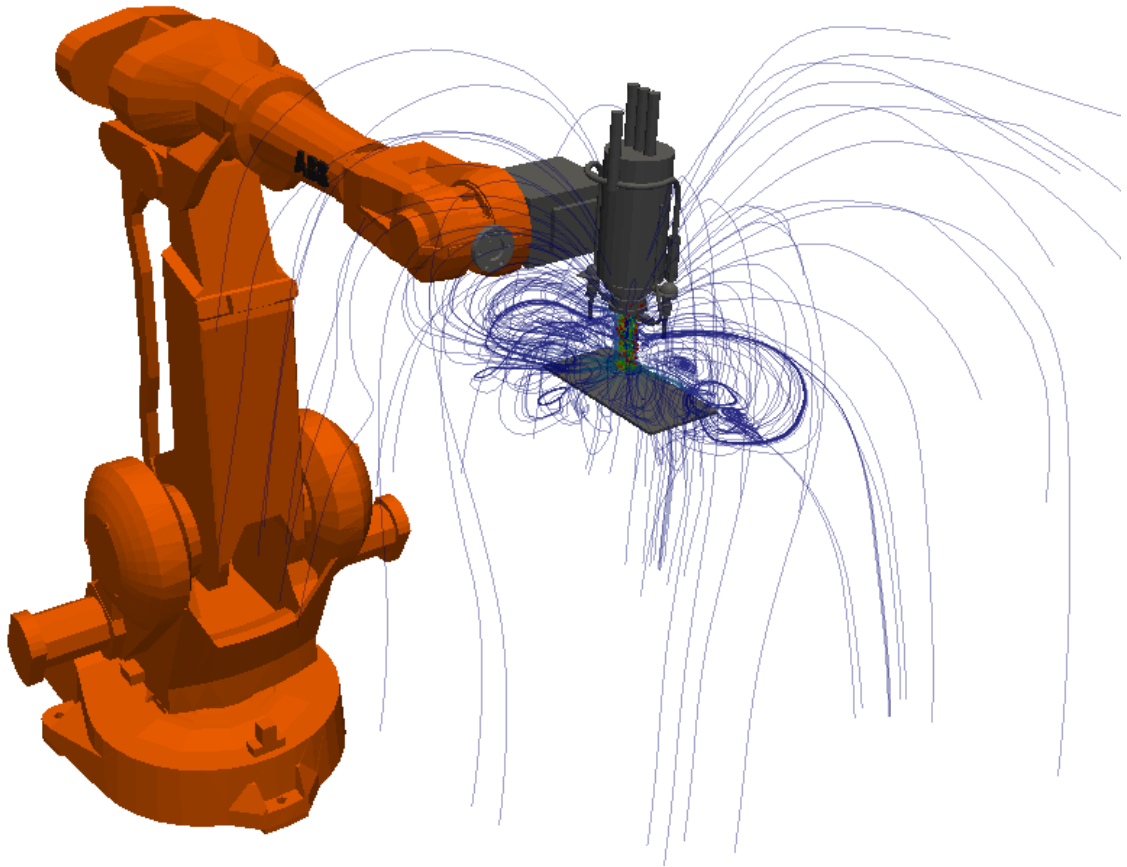


CHALMERS



Simulation of Thermal Spraying in IPS Virtual Paint

Master's Thesis in Solid and Fluid Mechanics

ANTON BERCE

Department of Applied Mechanics
Division of Fluid Mechanics
and Fraunhofer Chalmers Centre
CHALMERS UNIVERSITY OF TECHNOLOGY
Göteborg, Sweden 2011
Master's Thesis 2011:07

MASTER'S THESIS 2011:07

Simulation of Thermal Spraying in IPS Virtual Paint

Master's Thesis in Solid and Fluid Mechanics
ANTON BERCE

Department of Applied Mechanics
Division of Fluid Mechanics
and Fraunhofer Chalmers Centre
CHALMERS UNIVERSITY OF TECHNOLOGY
Göteborg, Sweden 2011

Simulation of Thermal Spraying in IPS Virtual Paint

ANTON BERCE

©ANTON BERCE, 2011

Master's Thesis 2011:07

ISSN 1652-8557

Department of Applied Mechanics

Division of Fluid Mechanics

and Fraunhofer Chalmers Centre

Chalmers University of Technology

SE-412 96 Göteborg

Sweden

Telephone: + 46 (0)31-772 1000

Cover:

Visualization of thermal spraying simulation including particles and streamlines, the geometries are the plasma gun mounted on a robot arm and the target plate.

Chalmers Reproservice
Göteborg, Sweden 2011

Simulation of Thermal Spraying in IPS Virtual Paint

Master's Thesis in Solid and Fluid Mechanics

Anton Berce

Department of Applied Mechanics

Division of Fluid Mechanics

and Fraunhofer Chalmers Centre

Department of Computational Engineering and Design

Abstract

The plasma spraying process is used to coat surfaces which are subjected to extreme conditions, e.g. rocket nozzles in the aerospace industry. The basic outline of the process is to inject metal or ceramic particles into a plasma jet generated by an electric arc. The particles are melted by the high temperature and accelerated towards the component to be coated (the substrate) by the high fluid velocities inside the plasma jet. When impacting on the substrate the particles solidify in a few milliseconds to form a strongly bonded coating.

At Fraunhofer Chalmers Centre a software for simulating electrostatic rotary bell spray painting is being developed and used in the automotive industry. In this thesis it has been investigated how well this software, IPS Virtual Paint, can predict a plasma spraying process.

Two test cases were defined and simulated. Data from previous detailed simulations of the plasma jet and its close surroundings was used to define the virtual plasma gun. Physical testing of the two cases was performed to calibrate and validate the results of the model. Also, a post-processing tool with the aim of calculating the coating thickness and temperature history of the coating and substrate was developed. The results from simulations and testing are compared and a satisfactory agreement has been reached.

Keywords: Plasma jet, Powder particles, Coating, Heat transfer, IBOFlow

Contents

Abstract	I
Contents	III
Acknowledgements	V
Nomenclature	VI
1 Introduction	1
1.1 Purpose	1
1.2 Limitations	1
1.3 Approach	2
1.4 Test cases	3
2 Theory	4
2.1 Electric arc wire spraying	4
2.2 Combustion Spraying	5
2.3 Plasma Spraying	5
2.3.1 Direct Current Arc Plasma Torch	7
2.3.2 Powders and Particle injection	8
2.3.3 Plasma jet and Particle's in-flight behaviour	10
2.3.4 Impact on substrate	12
2.4 IPS Virtual Paint	13
2.5 Air high temperature properties	13
2.5.1 Density	15
2.5.2 Viscosity	16
2.5.3 Thermal conductivity	16
2.5.4 Specific heat capacity	17
2.6 The Finite Volume Method on Conductive Heat Transfer	18
2.6.1 Governing Equation	18
2.6.2 Discretization	18
2.6.3 Boundary Conditions	20
3 Method	21
3.1 Input data	21
3.1.1 Defining the air injector	21
3.1.2 Defining the particle injector	24
3.2 Simulations	25
3.2.1 Calculation domain	25
3.2.2 Boundary Conditions	28
3.3 Solver settings	30
3.4 Postprocessing	31
3.4.1 splashHeat3D	31
4 Physical Testing	33
4.1 Test Case 1	35
4.2 Test Case 2	36

5	Results	37
5.1	Test Case 1	39
5.2	Test Case 2	40
5.2.1	Simulations	40
5.2.2	Comparison	42
5.3	Coating heat transfer solver	43
6	Summary and Conclusions	46
6.1	Input data	46
6.2	Simulations	47
6.3	Physical Testing	47
7	Future Work	48
	Appendix	51
A	Reference Case	51
B	2D Heat Equation	52
C	Test Case 3	54

Acknowledgements

This work was part of the project the Virtual Paint Factory within the FFI program for sustainable production funded by Vinnova. The research partners in the project are Volvo Cars, Saab Automobile, Scania, Volvo AB, Swerea IVF, General Motors and Fraunhofer-Chalmers Centre.

I would like to thank everyone at Fraunhofer Chalmers Centre (FCC), especially my supervisor Björn Andersson for all the support, guidance and interesting discussions he has given me during my master thesis work. Many thanks to Dr. Andreas Mark for all the help with the software IBOFlow and very interesting discussions about CFD. Also, I would like to thank Assoc. Prof. Fredrik Edelvik for trusting me with the responsibility, and giving me the confidence, to take on yet another new and exciting project. My time at FCC has been very rewarding and I have learned more than I could imagine. My fellow student Erik Svenning, with whom I have had the privilege to share an office, has also contributed greatly with good discussions and comments about work and life.

Thanks to Isabelle Choquet of University West for providing me with detailed knowledge about plasma spraying and for the data that laid the ground for all of my simulations.

Thanks to Prof. Lars Davidsson of the Dept. of Applied Mechanics, Division of Fluid Mechanics, for good courses during my master studies and guidance during my thesis work. I would also like to thank Esbjörn Jonasson of Kattegattgymnasiet, Halmstad, for opening my eyes to the world of mechanical engineering.

Last but not least I would like to thank Andreas Rudqvist, Krister Conradsson and Mats-Olov Hansson at Volvo Aero for sharing their knowledge about thermal spraying with me and for giving me the opportunity to perform physical testing of the process.

Göteborg June 2011
Anton Berce

Nomenclature

\dot{M}_c	Total mass flow of continuous phase
\dot{M}_d	Total mass flow of dispersed phase
\dot{Q}_J	Effective Joule heating
γ_r	Skewness of particle size distribution
\mathbf{Y}	Array of primitive variables
μ_c	Viscosity of the continuous phase
$\vec{\tau}$	Stress tensor
\vec{A}	Magnetic vector
\vec{B}	Magnetic field
\vec{J}_q	Current density
\vec{q}'	Total heat flux
\vec{u}	Velocity of the continuous phase
\vec{v}	Velocity of the dispersed phase
ϕ	Electric potential
ρ	Mass density
ρ_c	Density of the continuous phase
ρ_d	Density of the dispersed phase
σ	Surface tension
τ_F	Characteristic time scale of flow
τ_v	Particle momentum response time
C_p	Specific heat of continuous phase
D_p	Particle diameter
h	Convective heat transfer coeff
h	Equilibrium enthalpy
k_c	Thermal conductivity of continuous phase
k_p	Thermal conductivity of particle/droplet material
p	Pressure
R_{max}	Maximum radius of injection zone
R_{min}	Minimum radius of injection zone

T	Temperature
v_φ	Tangential velocity in applicator
v_r	Radial velocity in applicator
v_z	Axial velocity in applicator

1 Introduction

Applications where mechanical parts are subjected to extreme conditions, such as in the aircraft and aerospace technology, have developed a need for high performance coatings. When large aerodynamic, chemical, and/or thermal loads are subjected to part of a system it could fail due to erosion, corrosion and/or abrasion of its surface, sometimes with catastrophic effects.

Thermal spraying was introduced in the early 1900s and has evolved into a state of the art technology for producing qualitative coatings for a great range of applications. Several different techniques exist within the field, but the common denominator is that a solid material is molten and accelerated, towards the target surface, by a fluid jet. It is expected that the technique will continue to grow [8].

1.1 Purpose

The purpose of this thesis was to evaluate the possibilities of simulating thermal spraying by use of the existing software IPS Virtual Paint, developed by Fraunhofer Chalmers Centre, and to implement the necessary modifications to the software so that the dominant phenomena was captured. The goal of the project has been to perform simulations on test cases of which the results are comparable to measurements performed by Volvo Aero. Also, suggestions for further development are included.

1.2 Limitations

The project was limited in time due to the fact that this is a master thesis project. The work was carried out during the spring-semester of 2011 and finished in June 2011. The physical limitations, due to limiting computing- and time-resources are stated below:

- Only plasma spraying was considered in this project since this is the process used in the reference case (*Appendix A*).
- The simulations did not include the plasma torch. Hence the particles were assumed to be fully liquid at the inlet.
- The diameters and velocities at the inlet were assumed to be known and were based on the specifications given by the reference case.
- Simulations include only metal-alloy particles. Hence no ceramic particles.

1.3 Approach

For a CFD code to be industrially applicable it has to be quite fast, hence every detail of the jet-flow and particle impact has not been modeled in this work. Focus was put on the particle trajectories between the plasma torch and the substrate. The particle-substrate interaction was approximated with a simple model. In short, the steps can be described as follows:

1. The theory behind existing software was evaluated and compared to thermal spray theory, differences were located.
2. The existing software was slightly adapted to meet the new demands.
3. The simulations on test cases were performed and the results were compared to physical tests.
4. The most crucial areas for further development were located.

The scientific approach has been to perform an extensive study of the existing literature within the field and through careful consideration select and model the most dominant phenomena affecting the macro scale. An ongoing contact with the industrial partners was kept to ensure that the project remained on track and that the most relevant results were captured.

Below a short description of some previously performed simulations of the phenomena in the plasma spraying process is given.

Previous simulations of the thermal spraying process include work of Choquet [5] who performed detailed steady-state simulations of the plasma jet and its close surroundings with the aim of predicting the backflow of injected particles.

Li [10] modeled the high-velocity oxygen fuel (HVOF) process including a turbulent reacting flow field. Trelles [21] modeled the physics inside the plasma torch using a non-equilibrium model and an equilibrium model to compare the validity of the assumption of local thermodynamic equilibrium.

Marchand [12] investigated the interactions between the fluctuating plasma jet and the injected particles. In this study, a large eddy simulation (LES) was performed.

Ettouil [7] modeled the phase change for a particle inside a plasma jet. Both iron and zirconia particles were studied and it was found that ceramic particles have the tendency to experience inner temperature gradients whereas metallic particles tend to have a uniform inner temperature profile. Pasandideh-Fard [19] simulated the fluid flow, heat transfer and phase-change of a liquid particle impacting on a flat, solid, surface.

All of the above simulations are quite detailed and as far as the author of this thesis knows, there exist no tool to predict the macro scale of a thermal spraying process taking into account the movement of the geometries.

2 Theory

The different techniques of thermal spraying can be divided into three main groups. Each of these groups are presented in *Sections 2.1, 2.2 and 2.3* where focus is on plasma spraying since this is the process used in the reference case to this project.

2.1 Electric arc wire spraying

The general outline of a electric arc wire spraying process is shown in *Figure 2.1*. Two electrically conductive wires are fed into a point where they meet and melt due to the electric arc produced by the current passing through the wires. A stream of pressurized air is blown into the melting point and the molten material is atomized and accelerated towards the substrate. A stabilizing air stream surrounds the spray which prevents it from spreading too much into the atmosphere. The main application of the so called wire coats was originally protection against corrosion but now it is used for many other applications [8].

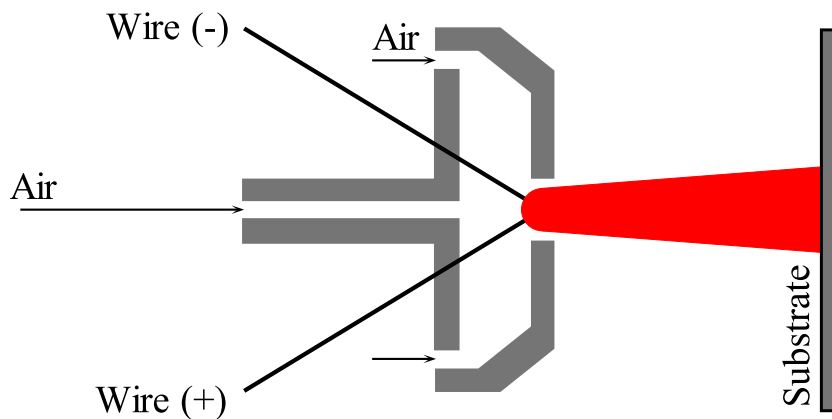


Figure 2.1: Basic outline of wire spraying

2.2 Combustion Spraying

This is a quite common technique where particles of metals, alloys or cermets are heated and propelled to a sonic/supersonic state in a combusting gas [10]. The ignition can be continuous or by a spark plug, the latter is the main difference between the Detonation-gun (D-gun, *Figure 2.2*) and the rest of the combustion-type heat sources.

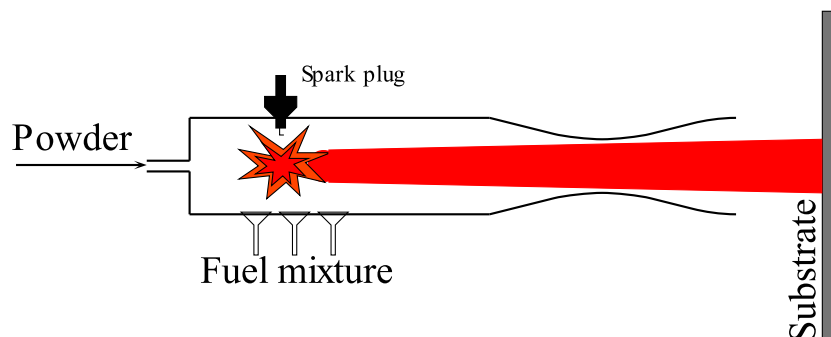


Figure 2.2: Basic outline of the detonation gun

The velocities can be varied to a great extent by use of different nozzles, for example the High Velocity Oxygen Fuel (HVOF) technique where a laval-type nozzle is used to accelerate the flow to a supersonic state. The outline of HVOF is drawn in *Figure 2.3*, HVOF has been widely used in the automotive, aerospace and chemical industries [10] to produce coatings with high resistance to wear, thermal loads or corrosion as well as coatings used as electrical insulators [2]. It is characterized by very high gas and particle velocities and relatively low temperatures, compared to plasma spraying.

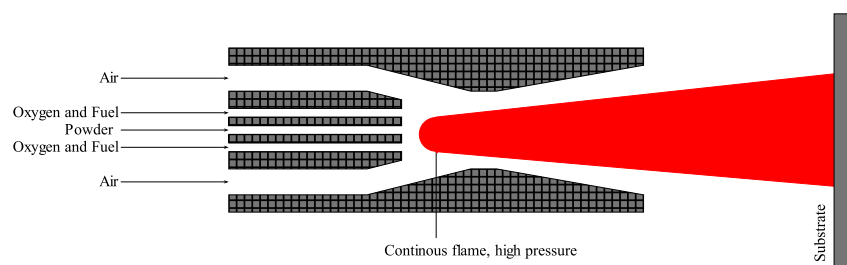


Figure 2.3: Basic outline of HVOF

2.3 Plasma Spraying

The process of plasma spraying is quite simple in its layout but the physics is rather complex. A better understanding of the underlying phenomena is needed to develop new coatings and to correlate the process parameters to the coating characteristics [11]. Below the process is divided into Direct Current Arc Plasma Torch, Powders and Particle injection, Plasma jet and Particle's in-flight behaviour and Impact on substrate.

In *Table 2.1* the most important dimensionless numbers are given. The typical values column indicates approximate values, particle in-flight region, in the plasma spraying process. The values in the right column are significantly different depending on whether the particle injection to the plasma core is studied or not.

Dimensionless number	Definition	Typical Values
<p>Fluid Reynolds number:</p> <p>L is a characteristic length of the flow (e.g. radius of plasma jet). The Reynolds number is an indication of the properties of the flowfield.</p>	$Re = \frac{\rho_c L \vec{u} }{\mu_c}$	10^6
<p>Relative Reynolds number:</p> <p>Based on particle to fluid relative velocity.</p>	$Re_r = \frac{\rho_c D_p \vec{u} - \vec{v} }{\mu_c}$	$50 - 100$
<p>Weber number:</p> <p>Particle dynamic pressure relative to surface tension. Indicates if the droplet will maintain a spherical shape, deform or break up. Low Weber numbers correspond to spherical droplets and breakup happens at $We \gtrsim 10$.</p>	$We = \frac{\rho_c D_p \vec{u} - \vec{v} ^2}{\sigma}$	< 1
<p>Biot number:</p> <p>The ratio between the surface- and internal heat transfer coefficients.</p>	$Bi = \frac{h D_p}{k_p}$	$0.01 - 10$
<p>Prandtl number:</p> <p>Ratio between viscous diffusion and thermal diffusion.</p>	$Pr = \frac{C_p \mu_c}{k_c}$	$0.7 - 0.8$
<p>Stokes number:</p> <p>The ratio between the momentum response time and a characteristic time scale of the flow. The timescale here is defined as the time from particle injection to impact (~ 0.001). Momentum response time is defined as</p> $\tau_v = \frac{\rho_d D_p^2}{18 \mu_c} \approx 0.01$ <p>τ_v is an indication of how quickly the particles respond to changes in the flowfield.</p>	$St_v = \frac{\tau_v}{\tau_F}$	~ 10
<p>Loading:</p> <p>The ratio of mass flux of the dispersed phase to that of the continuous phase.</p>	$Z = \frac{\dot{M}_d}{\dot{M}_c}$	$0.5 - 1$
<p>Sommerfeld number:</p> <p>Determines if a liquid particle will rebound, deposit or splash at the target surface. The Reynolds number used here is defined from particle density and viscosity [8].</p>	$K = \sqrt{We} \sqrt{Re}$	$0 - 1200$

Table 2.1: Dimensionless numbers

2.3.1 Direct Current Arc Plasma Torch

Plasma torches are very flexible instruments because of their wide temperature- and service characteristics range, the power level can differ as much as 1 - 10 000 kW [9] depending on the process. Most torches operate on direct current (DC) but there are examples of alternating current (AC) torches. The most essential parameters of the burner chamber and nozzle of a DC arc plasma torch are power supply, type of plasma forming gas or gases, mass flow rate of plasma gas, cooling, mass flow rate of cooling fluid, and nozzle geometry [11, 16].

A plasma torch has three main components; an anode, a cathode and the plasma forming gas. The plasma forming gas is usually a combination of two gases, e.g. Argon (Ar) or Helium (He). The anode, which in most cases consists of copper or copper alloys (sometimes with a tungsten insert) [9], is designed as a nozzle or tube that contains the plasma flame. The cathode is the most critical component in the plasma torch due to the high specific flux ratios. It is situated on the center-axis of the torch, see *Figure 2.4*, and the choice of cathode shape and material is determined by the plasma-forming gas and the specific enthalpy [9], but it usually consists of tungsten doped with thoriumdioxide ($W\ 2wt\% ThO_2$). A thorough discussion of materials is given in [9].

The plasma column is formed by electrons emitted from the cathode tip that are accelerated downstream by the electric field [11]. It should be noted that the flow inside a DC arc plasma torch is highly three-dimensional and unsteady despite of the relatively simple geometries and the steadiness of the boundary conditions. The three-dimensionality and unsteadiness due to an imbalance of the drag and electromagnetic forces [21].

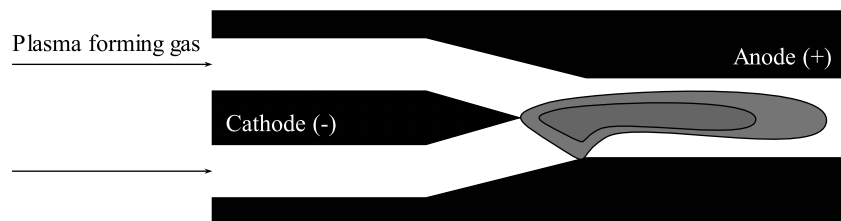


Figure 2.4: Basic outline of the plasma torch

When deriving equations for the plasma-flow an important assumption is made, namely the assumption of local thermodynamic equilibrium (LTE). LTE is the most common assumption in thermal plasma modeling [9] and it implies that all the chemical species (ions, electrons, atoms and molecules) within a fractional volume are in kinetic equilibrium. The validity of this assumption should be considered before applying a specific model to a system. Especially if strong interactions between the plasma and a stream of cold flow exist (for instance a protective boundary layer) [21], which is the case in many industrial applications. The equations in *Table 2.2* are the thermal plasma equations including conservation of (1) mass, (2) momentum, (3) thermal energy, (4) electrical current and (5) the magnetic induction equation [21] when the LTE assumption is valid.

i	\mathbf{Y}_i	<i>Transient</i>	<i>Advective</i>	<i>Diffusive</i>	<i>Reactive</i>
1	p	$\frac{\partial \rho}{\partial t}$	$\vec{\mathbf{u}} \cdot \nabla \rho + \rho \nabla \cdot \vec{\mathbf{u}}$	0	0
2	$\vec{\mathbf{u}}$	$\rho \frac{\partial \vec{\mathbf{u}}}{\partial t}$	$\rho \vec{\mathbf{u}} \cdot \nabla \vec{\mathbf{u}} - \nabla p$	$-\nabla \cdot \vec{\boldsymbol{\tau}}$	$\vec{\mathbf{J}}_q \times \vec{\mathbf{B}}$
3	T	$\rho \frac{\partial h}{\partial t}$	$\rho \vec{\mathbf{u}} \cdot \nabla h$	$-\nabla \cdot \vec{\mathbf{q}}'$	$\frac{Dp}{Dt} + \dot{Q}_J - \dot{Q}_r$
4	ϕ	0	0	$-\nabla \cdot \vec{\mathbf{J}}_q$	0
5	$\vec{\mathbf{A}}$	$\rho \frac{\partial \vec{\mathbf{A}}}{\partial t}$	$\nabla \phi - \vec{\mathbf{u}} \times \nabla \times \vec{\mathbf{A}}$	$\eta \nabla^2 \vec{\mathbf{A}}$	$\vec{\mathbf{0}}$

Table 2.2: Thermal plasma equations

In *Table 2.2*, p is the pressure, $\vec{\mathbf{u}}$ velocity vector, T temperature, ϕ electric potential and $\vec{\mathbf{A}}$ the magnetic vector. ρ is the mass density, t time, $\vec{\boldsymbol{\tau}}$ the stress tensor, $\vec{\mathbf{J}}_q$ current density, and $\vec{\mathbf{B}}$ the magnetic field. The equations in *Table 2.2* will not be solved in this project and are given for the sake of completeness. A review can be found in [21] where they are solved using a variational multi-scale finite element method.

2.3.2 Powders and Particle injection

The extremely wide temperature range of plasma spraying makes it possible to use almost any metallic or non-metallic material such as oxides, carbides, nitrides, borides, silicides, metallics mixed with ceramics and even plastics, in form of powder. The selection of powder depends on the desired coating characteristics [16]. The temperatures in the plasma core can exceed 30 000 K [9] contributing to the flexibility of the process.

Wear resistance (bearings, cog wheels), thermal resistance (turbines, engine parts, rocket nozzles), corrosion resistance (offshore equipment, bridges), electrical conductivity and resistance (conductors or insulators), renovation of surfaces and worn out parts (renovation of expensive turbine rotors and crankshafts) are some of the applications for different kinds of materials. In the reference case in *Appendix A* a powder consisting of Nickel and Aluminium is used (Ni-5wt%Al) and the particle diameters are approximately 65 μm .

Given a plasma nozzle flow the next important issue is the injection of the particles. The time spent by a particle inside the plasma jet is referred to as the residence time. This is an important parameter since a small difference in residence time has huge impact on particle temperature and total heat flux. This parameter can be controlled in a number of ways, e.g. changing the position of injection or type of injector [22], or changing the angle and velocity of injection [11]. One or several injection tubes can be used. In the reference case of *Appendix A* one injection tube perpendicular to the plasma jet is used which is situated 5 mm downstream of the plasma gun exit. *Figure 2.5* illustrates some of the particle injection parameters.

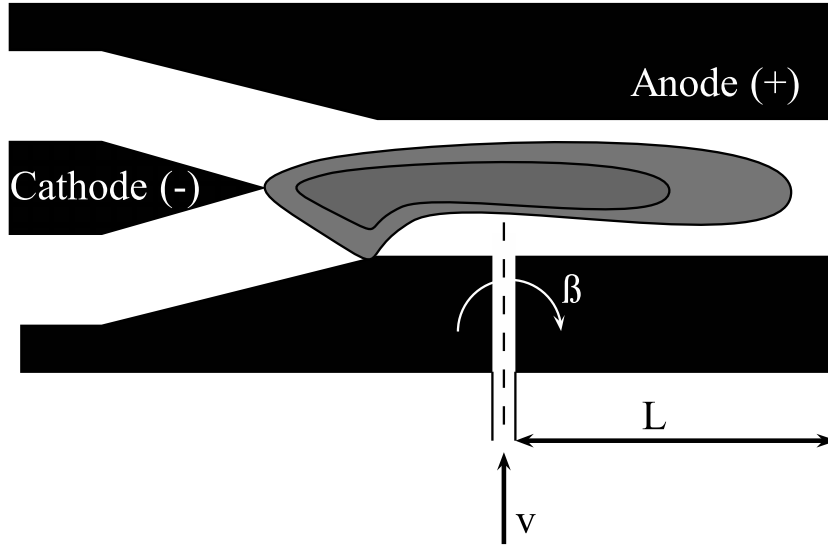


Figure 2.5: Injection parameters

In *Figure 2.5* L defines the position of particle injection. If $L \leq 0$ the injection occurs at the nozzle exit or just downstream of it. β is the injection angle and v is the injection velocity. These three parameters must be optimized, in accordance with several more, for every specific application and the industry today relies on the experience and knowledge of the operators. In most cases, a high density gas, such as Argon or Nitrogen, is used as a carrier gas of the particles in the injection tube [22] but the particles can also be suspended in a liquid that is injected into the plasma [12].

In the reference case 4 standard litres per minute (slpm) of argon is used as carrier gas for the powder particles and $\dot{m}_p = 54$ g/min particles is fed into the plasma jet. The powder injector diameter is 1.8 mm which corresponds to an injection velocity of approximately 26 m/s. The density of the powder $\rho_{powder} = 0.95\rho_{Ni} + 0.05\rho_{Al} = 8590$ kg/m³. If the mean radius of the particles is 30 μ m then the volume

$$V_p = \frac{4}{3}\pi r^3 = 1.131 \cdot 10^{-13} \text{ m}^3$$

which gives the mean mass of the particles

$$m_p = 9.715 \cdot 10^{-10} \text{ kg}$$

Hence $\frac{\dot{m}_p}{m_p} \simeq 9.26 \cdot 10^5$ particles are injected per second.

As soon as the particles are injected, in- or outside the plasma, they are affected by the extreme temperatures and high velocity. The authors of [22] defined the residence time t_r as the time spent, by a particle, inside the hot core of the plasma. In [7] it was stated that for *Biot numbers* < 0.1 (see *Table 2.1*) which is the case for metal alloy particles, the lumped heat capacity method can be assumed. This assumption implies that there are no internal temperature gradients in the particle.

2.3.3 Plasma jet and Particle's in-flight behaviour

Once melted and accelerated in the torch, the particles are transported towards the substrate. This is the part that will be simulated in this project and it is key to find the dominating phenomena of the fluid-particle flow in this region.

When the particles are travelling downstream the surrounding fluid will have a higher concentration of air, lower temperature and lower velocity than close to the plasma gun exit. There are many ongoing phenomena, such as particle oxidation and particle dispersion due to turbulence, in the region between the plasma gun and the point of impact. The oxidation of particles is not taken into account in this project and the dispersion due to turbulence is taken into account through a random factor affecting the particle velocity and direction upon injection, described in *Section 3.1.2*.

The local loading is defined as the mass flux ratio between the dispersed phase and the continuous phase [6]. The definition can be found in *Table 2.1*. This is an important parameter to consider when determining if one-way, two-way or four-way coupling should be used to model the fluid-particle interaction. One-way coupling implies the assumption that the continuous phase affects the dispersed phase in terms of drag force, energy transfer etcetera, but the presence of the dispersed phase does not affect the fluid. Two-way coupling implies that the dispersed phase affect the continuous phase through momentum, mass and/or energy transfer and vice versa. Four-way coupling adds the particle-particle interaction to the list of what should be considered.

Generally, a small loading implies that one-way coupling can be assumed for the momentum and energy coupling, and mass coupling can be neglected. In [12] one-way coupling is assumed and the particles are injected just outside the plasma-torch. In the case specified in *Appendix A* the loading is $Z \approx 0.9$. In the fluid flow solver of IPS Virtual Paint (IBOFlow), two-way coupling is standard and no attempts to model the thermal spraying process using one-way coupling will be made.

The definitions of averaging are stated in *Table 2.3*.

Type	Definition
Volume average:	$\bar{B} = \frac{1}{V} \int_V B dV$
Phase average:	$\langle B \rangle = \frac{1}{V_c} \int_{V_c} B dV$
Mass average:	$\tilde{B} = \frac{1}{\langle \rho_c \rangle} \frac{1}{V_c} \int_{V_c} \rho_c u_i dV$

Table 2.3: Definitions of averaging

The governing equations for the fluid flow are given in the Eulerian framework and hence they are field equations. They are the continuity equation 2.1, the momentum equation 2.2, and the thermal energy equation 2.4 [6]. Compared to the equations in *Table 2.2* this part of the domain does not consider the magnetic fields and chemical reactions in the same detail. The equations consider one continuous phase, hence if several species are

present mixing models for the transport properties can be used [18]. Subscript c and d are indications of continuous and dispersed phase and the subscript i indicates the cartesian coordinate directions.

$$\frac{\partial}{\partial t}(\alpha_c \langle \rho_c \rangle) + \frac{\partial}{\partial x_i}(\alpha_c \langle \rho_c \rangle \tilde{u}_i) = S_{mass} \quad (2.1)$$

The last term S_{mass} is referred to as the mass phase coupling term. If $S_{mass} = 0$ in [Equation 2.1](#) there is no mass transfer between the phases. Hence the particles are assumed not to evaporate.

$$\begin{aligned} \frac{\partial}{\partial t}(\alpha_c \langle \rho_c \rangle \tilde{u}_i) + \frac{\partial}{\partial x_j}(\alpha_c \langle \rho_c \rangle \tilde{u}_i \tilde{u}_j) &= -\frac{1}{V} \sum_k v_{i,k} \dot{m}_k - \frac{\partial}{\partial x_i} \langle p \rangle \\ &+ \frac{\partial}{\partial x_j} \langle \tau_{ij} \rangle - \frac{\partial}{\partial x_j}(\alpha_c \langle \rho_c \delta u_i \delta u_j \rangle) - \frac{1}{V} \sum_k F_{i,k} + \alpha_c \langle \rho_c \rangle g_i \end{aligned} \quad (2.2)$$

[Equation 2.2](#) is general and includes the phase coupling through the volume fraction α_c and the forces exerted on the fluid by the dispersed phase F_i [6]. $v_{i,k}$ is the velocity of particle k , \dot{m}_k the evaporation rate of droplet k , and the stress tensor according to [Equation 2.3](#).

$$\tau_{ij} = \mu \left(\frac{\partial u_i}{\partial x_j} + \frac{\partial u_j}{\partial x_i} \right) \quad (2.3)$$

Since large temperature gradients is a key phenomenon in plasma spraying, the energy equation needs to be solved in order to capture the physics of the system. [Equation 2.4](#) below is the thermal energy equation. In [6] a thorough derivation of the energy equation can be found. In [Equation 2.4](#) \tilde{i}_c and \tilde{h}_c are the mass averaged specific internal energy and the mass averaged enthalpy.

$$\begin{aligned} \frac{\partial}{\partial t}[\alpha_c \langle \rho_c \rangle \tilde{i}_c] + \frac{\partial}{\partial x_i}[\alpha_c \langle \rho_c \rangle \tilde{u}_i \tilde{h}_c] &= \underbrace{\tilde{u}_i \alpha_c \frac{\partial}{\partial x_i} \langle p \rangle}_a \\ - \underbrace{\sum_n \dot{m}_k \left(h_{s,k} + \frac{|v_{i,k} - \tilde{u}_i|^2}{2} + \frac{w_k^2}{2} \right)}_b &+ \underbrace{\frac{3\pi\mu_c}{V} \sum_k D_k f_k |\tilde{u}_i - v_{i,k}|^2}_c \\ - \underbrace{\langle p \rangle \frac{\partial}{\partial x_i}(\alpha_d \langle v_i \rangle)}_d &+ \underbrace{\frac{1}{V} \sum_k \dot{V}_{d,k} p_{s,k}}_e + \underbrace{\langle \tau_{ij} \rangle \left[\frac{\partial}{\partial x_j}(\alpha_d \langle v_i \rangle + \alpha_c \tilde{u}_i) \right]}_f \\ &+ \underbrace{\frac{\partial}{\partial x_i} \left(k_{eff} \frac{\partial \langle T_c \rangle}{\partial x_i} \right)}_g + \underbrace{\frac{2\pi k_c}{V} \sum_k \left(\frac{Nu}{2} \right)_k D_k (T_{d,k} - \langle T_c \rangle)}_h \end{aligned} \quad (2.4)$$

The meaning of each term in the right hand side of [Equation 2.4](#) is given in [Table 2.4](#). The left hand side contains the transient and convective terms.

The particles are usually treated in the Lagrangian framework. Hence they are discrete elements free to take any position inside the domain. The particles are suspended in the continuous phase, which is often referred to as the carrier phase, and the dynamics of them

- | |
|---|
| <ul style="list-style-type: none"> (a) Reversible work (b) Energy influx due to evaporation of the dispersed phase, \dot{m}_k is the rate of change of particle k's mass, $h_{s,k}$ is the enthalpy of the continuous phase at the surface of particle k and w'_k is the velocity of the continuous phase, w.r.t. the particle center, at the surface of the particle k (0 if no slip and solid boundary) (c) Energy dissipation from the particle-fluid interaction (d) Flow work due to motion of the dispersed phase (e) Work rate associated with droplet expansion, $\dot{V}_{d,k}$ and $p_{s,k}$ are the expansion rate and pressure on surface of particle (f) Energy dissipation due to shear stress in the continuous phase (g) Heat transfer through the mixture, $k_{eff} = \alpha_c k_c + \alpha_d k_d$ is the effective thermal conductivity of the continuous phase (h) Heat transfer from the dispersed phase, Nu is the <i>Nusselt Number</i> |
|---|

Table 2.4: Terms in *Equation 2.4*

is determined by Newton's second law through a set of forces acting on them. The forces include the drag, lift, gravity, buoyancy, pressure gradient, Basset and thermophoretic forces etcetera and before neglecting any force one has to motivate why.

Also, the particles are affected by the temperature of the surrounding fluid and the solutions to the governing transient heat-transfer equations are far from trivial since the boundary layer of the particle may have strong variations in fluid properties due to the large temperature gradients present. The *Biot number* is a key dimensionless number when determining if there are large inner temperature gradients in the particle and it is defined as the ratio between the particle's and the plasma's thermal conductivities, *Table 2.1*. A rule of thumb is that for $Bi < 0.1$ a uniform inner temperature distribution of the particle can be assumed [9]. Metals can often be assumed to have a uniform temperature distribution whereas ceramics can have large inner temperature gradients. In [7] an iron and a zirconia particle were compared and it was found that the iron particle had an almost negligible temperature variation which allows the assumption of lumped-heat capacity, but the ceramic particle was found to have very large temperature gradients.

2.3.4 Impact on substrate

The impact of a particle on a surface is a very complex process. In addition to fluid flow and heat transfer the modeling includes free surfaces of the particles undergoing large deformations and moving liquid-solid contact lines [19]. To fully solve the impact of several particles in a thermal spray process is not possible with the computing resources available today; the impact of one tin particle on an inclined plane was modeled in [19] and the

CPU time was in the order of days. Hence simplifications must be made. Many models assume that the particle has a disk-shaped splat when impacting on the substrate, and the diameter of the splat is estimated by the particle Reynolds number prior to the splat [11, 8]. A governing dimensionless number is the *Sommerfeld number*, K , defined in [Table 2.1](#). $K < 3$ corresponds to particle rebound, $3 < K < 58$ to particle deposition and $K > 58$ to particle splashing on the target surface.

Once the particles have impinged on the substrate they bond to form the coating. The main bonding forces are (1) Mechanical anchorage, (2) Van der Waals-type forces, (3) Chemical reactions, i.e. covalent bonds and (4) Metallurgic processes that form microwelds [16].

The surface preparation prior to spraying has a large impact on the coating strength. Parameters such as surface roughness and cleanness can be altered through e.g. blasting. Also, if the coefficients of thermal expansion of the particles and the substrate differ a lot, an interlayer can be sprayed to prevent stresses in the surface. This is especially important to consider when spraying ceramic particles on a metal surface [16]. Interlayers are also used to get better adherence in coatings. The powder used in the reference case in [Appendix A](#) is normally used by Volvo Aero as an interlayer [5].

2.4 IPS Virtual Paint

IPS Virtual Paint is a software package developed by *FCC* including simulation set up, fluid flow solver and particle tracer (IBOFlow), and post processing tools such as ray-tracing and visualization [15, 13]. It is the result of an ongoing research project in which several industrial partners¹ are involved and the software is continuously updated. The software allows the user to simulate the spray painting process from setup to solving and post processing, all in one interface.

IBOFlow uses a finite volume discretization to solve the fluid flow around immersed bodies which can be static or moving. It implements several immersed boundary methods such as the hybrid method and the mirroring immersed boundary method [14]. The applications of IBOFlow include DNS-simulations of particle flow, paper forming, spray painting etc. The particles are traced in the Lagrangian framework and two-way coupling including all the forces mentioned in [Section 2.3.3](#). IBOFlow also includes a solver of the energy equation and in this project, a minor additional package was added to accurately capture the behaviour of the fluid at temperatures where the properties of the fluid shift due to dissociation.

2.5 Air high temperature properties

The temperature difference between the nozzle exit and the substrate is of the order of 10^4 K, therefore changes in the properties of the continuous phase due to dissociation and ionization need to be considered. At temperatures above 2500 K the O_2 -molecules will start to dissociate, which means that the O-atoms will start to break loose from the molecules. At 4000 K the N_2 molecules will start dissociating and above 9000 K the electrons will start breaking loose from the atoms [1], in other words ionization will start. Nylén [18] developed a CFD model which calculates the properties of the mixture according to mixing

¹Volvo Car Corporation, GM, Saab Automobile AB, Swerea

rules given in *Table 2.5* below. In the testcase specified in *Appendix A* the temperature of the continuous phase is above 13 000 K.

$$\begin{aligned}
 C_p(T) &= \sum_i C_{p,i}(T)x_i \\
 H(T) &= \sum_i H_i(T)x_i \\
 \mu(T) &= \sum_i \frac{\mu_i(T)}{1 + \sum_{j \neq i} \Phi_{ij} \frac{y_j}{y_i}} \\
 k(T) &= \sum_i \frac{k_i(T)}{1 + \sum_{j \neq i} A_{ij} \frac{y_j}{y_i}} \\
 \Phi_{ij} &= \frac{1}{\sqrt{8}} \left[1 + \left(\frac{\mu_i}{\mu_j} \right)^{\frac{1}{2}} \left(\frac{M_j}{M_i} \right)^{\frac{1}{4}} \right]^2 \left[1 + \left(\frac{M_i}{M_j} \right) \right]^{-\frac{1}{2}} \\
 A_{ij} &= 1.065 \Phi_{ij}
 \end{aligned}$$

Table 2.5: Mixing rules for physical properties

Since the properties of each part of the mixture is temperature dependent a database of $C_p(T)$, $\mu(T)$ and $k(T)$, $T_{min} < T < T_{max}$ for each component in the mixture is needed to determine the correct properties of the mixture.

In this thesis the continuous mixture will be approximated by air and its chemical sub-species. At high temperatures the properties of air will not remain constant. As temperature increases the gas molecules will start to vibrate and eventually break loose into dissociation. In a thermal plasma the gases are ionized and hence electrically conductive.

In [3] the properties of air at atmospheric pressure and in the temperature range 50 to 30 000 K are presented. The tables are calculated through collision integrals of several species of nitrogen and oxygen, their ions and electrons. The tables have been used to modify the fluid flow solver used in this work, and the data from the tables are given and briefly discussed below.

An interpolation routine which, given the fluid temperature, interpolates in the tables has been written in *C++* and merged with IBOFlow. The routine is based on *Cubic spline interpolation* [20] and it returns interpolated data in which the second derivative is continuous between intervals.

The cubic spline interpolation routine approximates the function with a third order polynomial resulting in a system of equations which in turn leads to a tri-diagonal matrix to be solved. A Tri-Diagonal Matrix Algorithm (TDMA) solver was implemented in the *C++* package according to the theory in [23]. All figures of this section shows the original data, the cubic spline interpolation and *Matlab's* built-in spline interpolation routine.

2.5.1 Density

The density of air decreases with increasing temperature. The *perfect-gas law* is stated in *Equation 2.5*. It relates pressure, density and temperature through the gas constant. If a gas is held at constant pressure while temperature increases, ρ must decrease if R is constant. At room temperature conditions, the density of air is $\rho \sim 1.2$ [kg/m³].

$$p = \rho RT \quad (2.5)$$

The definition of the *gas constant* R is $R = \frac{R_u}{M}$ [4] where R_u is the universal gas constant (same for all substances) and M is the molar mass. Hence, if the molar mass is constant, density must decrease with increasing temperature, as can be seen in *Figure 2.6*. It can be seen that for temperatures $T \gtrsim 2500$ K the ideal gas law is no longer valid, because the O_2 -molecules starts to dissociate. When the molecules split up the species are less closely packed. The ideal gas law assumes that all molecules remain intact, hence the difference.

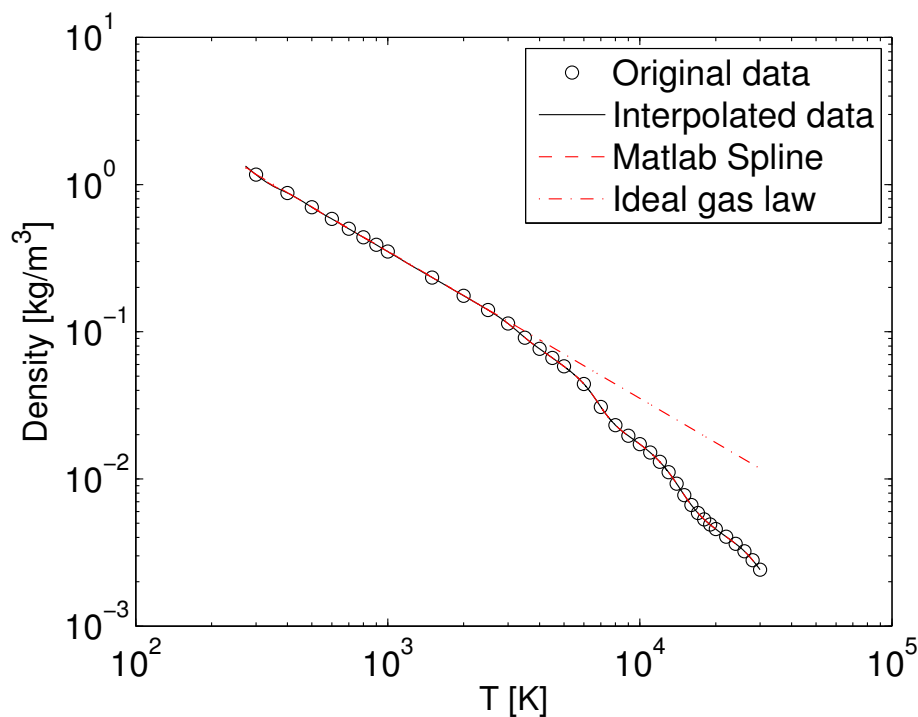


Figure 2.6: Density of high temperature air

2.5.2 Viscosity

The viscosity of high temperature air increases nearly linearly up to the first point of ionization. At temperatures above 10^4 K it decreases due the increase of free electrons and the increase of collision integrals for ion-ion interaction [3]. In the figure below the tables of [3] have been interpolated with the cubic spline interpolation routine.

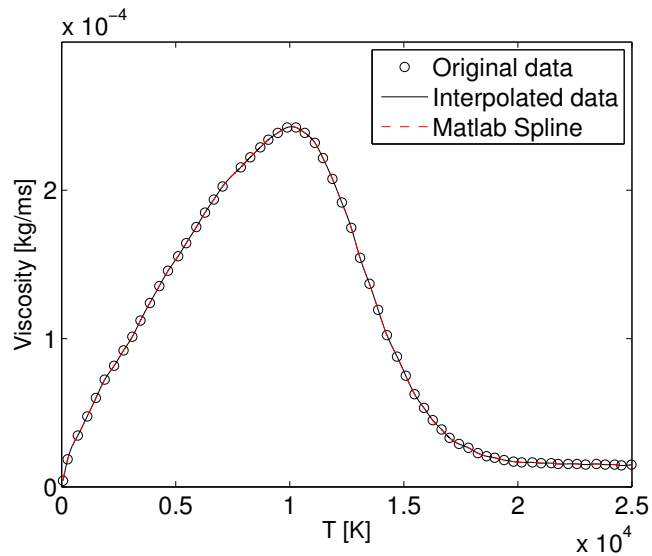


Figure 2.7: Viscosity of high temperature air

2.5.3 Thermal conductivity

In *Figure 2.8* the thermal conductivity is plotted as a function of temperature. The peaks are due to chemical reactions taking place, which release internal energy [3].

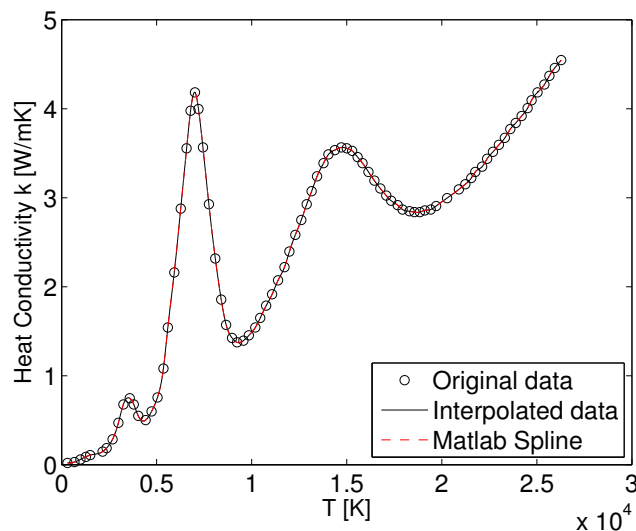


Figure 2.8: Thermal conductivity of high temperature air

2.5.4 Specific heat capacity

The specific heat capacity is, as implied by the unit J/kgK, the amount of heat needed to change the temperature of a 1kg body, or fluid element, by one degree. In the figure below a difference between *Matlab's* spline and the implemented cubic spline interpolation routine can be seen, which is due to a difference in the boundary conditions used when solving the system of equations to find the third order polynomial describing the interpolated function.

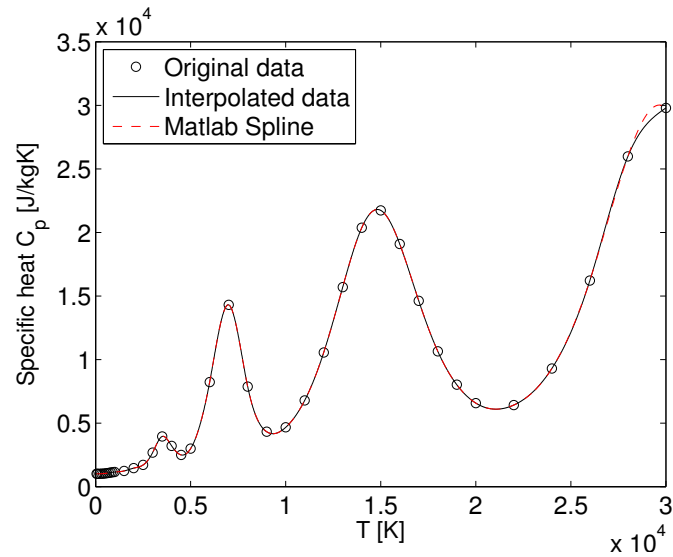


Figure 2.9: Specific Heat Capacity of high temperature air

2.6 The Finite Volume Method on Conductive Heat Transfer

In this section an overview of the Finite Volume Method is given with the aim of solving the three dimensional conductive heat transfer equation. The theory has been used to develop the software described in *Section 5.3*. In *Section 2.6.1* the conductive heat transfer equation is given, in *Section 2.6.2* it is discretized using the finite volume method and in *Section 2.6.3* the boundary conditions are described.

2.6.1 Governing Equation

In a general solid material the conduction of heat is described by *Equation 2.6*. The equation is parabolic and derived from Fouriers law and conservation of energy. There exists several analytical solutions for certain sets of boundary conditions, one of these analytical solutions is derived in *Appendix B*. It is used for validation of the coating heat transfer solver developed in this work.

$$\rho C_p \frac{\partial T}{\partial t} = \nabla \cdot (k \nabla T) \quad (2.6)$$

where ρ is the mass density [kg/m³], C_p is the specific heat capacity [J/kgK] and k is the thermal conductivity [W/mK]. The thermal conductivity is in this case not assumed to be constant since several species of materials will be present while solving the equation for the particle impacts (*Section 3.4.1*). Note that no convection is present in the governing equation, and thus the particles are assumed to solidify instantly on impact.

2.6.2 Discretization

The calculation domain is divided into small cells in which all properties are assumed to be constant. The data is stored in the discrete locations of the cell centers and the transport of energy is calculated as fluxes on the cell faces. This makes the scheme conservative since the flux entering the cell is by definition equal to the flux leaving the neighbouring cell.

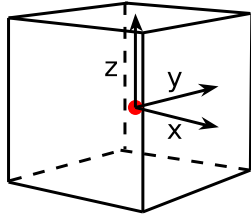


Figure 2.10: A finite volume cell

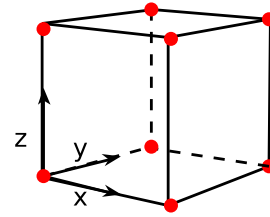


Figure 2.11: A finite element cell

Equation 2.6 is discretized by integrating over the control volumes and in time according to *Equation 2.7*.

$$\int_t \int_V \rho C_p \frac{\partial T}{\partial t} dV dt = \int_t \int_V \nabla \cdot (k \nabla T) dV dt \quad (2.7)$$

The time-integrals can be approximated with one of three methods; Implicit Euler, Explicit Euler or a mixture of the two. In [15] a mixing constant $0 \leq f \leq 1$ is introduced such that

$$\int_t^{t+\Delta t} T dt = (fT + (1-f)T^0)\Delta t \quad (2.8)$$

$f = 0$ corresponds to the explicit scheme where only values of the old temperature will appear on the right hand side, and hence the equation can be solved explicitly. $f = 1$ gives the implicit scheme where only values of the temperature at time $t + \Delta t$ appear. This leads to a system of equations that must be solved by matrix inversion. The implicit scheme is however unconditionally stable which enables larger timesteps. If $f = \frac{1}{2}$ the Crank Nicolson scheme is used. In this work the implicit approach will be used for the time discretization.

The spatial integrals are approximated by making use of the divergence theorem which states that the change inside of a volume is equal to the sum of fluxes over the surface of the volume. Thus, the transport coefficients, which are stored in the cell center, must be interpolated to the cell faces. The linear interpolation on a non uniform grid is implemented in the software described in *Section 5.3*. The face properties are approximated through weighting the cell-centered properties with the inverse distance to the face. In this section however, a uniform grid will be assumed for simplicity.

The left hand side of *Equation 2.7* is approximated as

$$\bar{\rho}\bar{C}_p(T_P - T_P^0)\Delta V$$

where $\bar{\rho}$ and \bar{C}_p are the average density and specific heat capacity inside the volume. The subscript P indicates the cell centered position and superscript 0 indicates the old value. Hence T_P^0 is the old, cell centered temperature.

The *Laplace* term of *Equation 2.7* is approximated as

$$\left[\frac{k_e \frac{dT}{dx} \Big|_e - k_w \frac{dT}{dx} \Big|_w}{\Delta x} + \frac{k_n \frac{dT}{dy} \Big|_n - k_s \frac{dT}{dy} \Big|_s}{\Delta y} + \frac{k_t \frac{dT}{dz} \Big|_t - k_b \frac{dT}{dz} \Big|_b}{\Delta z} \right] \Delta t \Delta V \quad (2.9)$$

The subscripts w, e, s, n, b and t represent the cell face properties for the west, east, south, north, bottom and top face. The upper case letters below refer to the neighbouring cell centered properties. The derivatives are evaluated at the cell faces as

$$\begin{aligned} \frac{dT}{dx} \Big|_w &= \frac{T_P - T_E}{\Delta x} & \frac{dT}{dx} \Big|_e &= \frac{T_E - T_P}{\Delta x} \\ \frac{dT}{dy} \Big|_s &= \frac{T_P - T_S}{\Delta y} & \frac{dT}{dy} \Big|_n &= \frac{T_N - T_P}{\Delta y} \\ \frac{dT}{dz} \Big|_b &= \frac{T_P - T_B}{\Delta z} & \frac{dT}{dz} \Big|_t &= \frac{T_T - T_P}{\Delta z} \end{aligned} \quad (2.10)$$

$$\Delta V = \Delta x \Delta y \Delta z \Rightarrow$$

$$\begin{aligned} a_w &= \frac{k_W + k_P}{2\Delta x} A_w & a_e &= \frac{k_E + k_P}{2\Delta x} A_e \\ a_s &= \frac{k_S + k_P}{2\Delta y} A_s & a_n &= \frac{k_N + k_P}{2\Delta y} A_n \\ a_b &= \frac{k_B + k_P}{2\Delta z} A_b & a_t &= \frac{k_T + k_P}{2\Delta z} A_t \end{aligned} \quad (2.11)$$

where A_x is the cell face area of face x . If

$$a_p = \bar{\rho} \bar{C}_p \frac{\Delta V}{\Delta t} + a_w + a_e + a_s + a_n + a_b + a_t$$

the discrete heat equation reduces to

$$a_p T_p - a_w T_w - a_e T_e - a_s T_s - a_n T_n - a_b T_b - a_t T_t = \bar{\rho} \bar{C}_p \frac{\Delta V}{\Delta t} T_p^0 + \bar{q} \Delta V \quad (2.12)$$

2.6.3 Boundary Conditions

Boundary conditions are used to close the systems of equations and in [15], the general Robin boundary condition *Equation 2.13* is given

$$AT_\gamma + B \frac{\partial T_\gamma}{\partial n} = C \quad (2.13)$$

where T_γ is the temperature on the boundary, A , B and C are constants determining the type of boundary condition and its value, n is the normal direction to the boundary.

The Neumann boundary condition is obtained by setting $A = 0$ and $B = 1$, thus prescribing the flux over the boundary. The special case of $C = 0$ corresponds to the homogeneous Neumann boundary condition in which the flux over the boundary is zero.

By setting $A = 1$ and $B = 0$ in *Equation 2.13* a Dirichlet-type boundary condition is obtained, prescribing the value of the temperature on the cell face. Note that no part of the boundary contains cell-centers, but only cell-faces. The boundary is hence not part of the solution in a Finite Volume approach, contrary to the Finite Element Method where the data is stored in the cell nodes as illustrated by *Figures 2.10* and *2.11*. In the finite volume method the boundary temperature enters the equations as ghost cells.

3 Method

The complexity of the underlying physics of plasma spraying has prevented the theory to be industrially applicable. Since the aim of this project is to satisfy the need of a reliable and relatively fast tool for predicting the coating characteristics idealization of the theory has to be made. In this chapter this simplified model is described and an argumentation to why this model is adequate is given.

3.1 Input data

Dr. Choquet of University West has made several detailed studies of the plasma spraying process, one of which has been used in this work, to define an applicator used in the IPS Virtual Paint simulations. In *Figure 3.1* the axial velocity of the plasma jet is displayed, where the velocity reaches almost 3000 m/s in the core of the plasma.

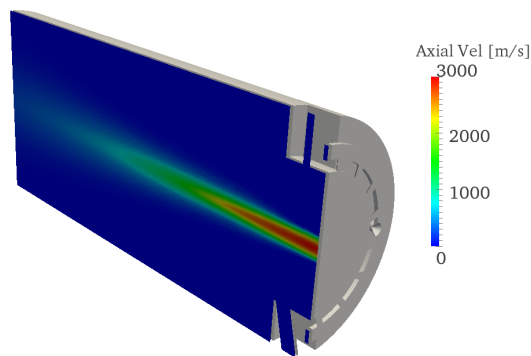


Figure 3.1: The plasma jet from Uni. West, axial velocity [5]

The simulations were performed by Dr. Isabelle Choquet using the commercial software Ansys Fluent and the calculation domain, with diameter 50 mm and length 120 mm, consists of above 4 million cells. The fluid was assumed to consist of three species: Plasma gas (ionized argon and hydrogen), pure argon as carrier gas for the particles and air in the surroundings. The compressible, turbulent flow equations were closed by the Boussinesq assumption and Reynolds decomposition. The turbulent terms were modeled by the RNG $k - \varepsilon$ model [5].

The validity of the model should be discussed. The $k - \varepsilon$ turbulence model is used which limits the accuracy. The viscosity of the fluid is calculated from the ideal gas law, which is not valid for all temperatures in the domain (seen *Section 2.5*). However the purpose of this section is to explain a method to use existing detailed simulations to define an applicator in IPS Virtual Paint.

3.1.1 Defining the air injector

IPS Virtual Paint uses paint applicators to define the spray guns. Several injection zones, each containing the velocities of air and paint, are specified leading to a great flexibility in simulation set-up. If the flow of paint is set to zero in an injection zone the zone will not add any paint particles and thus defining an air-injector. Since the particles in a plasma spraying process are injected in an angle to the plasma jet the paint flow is not

axisymmetric and hence several applicators has to be used to model the plasma gun; one air-injector and one or more particle injectors (depending on whether one or more particle injectors are used in the real plasma gun). In the reference case defined in *Appendix A* one injection zone is used.

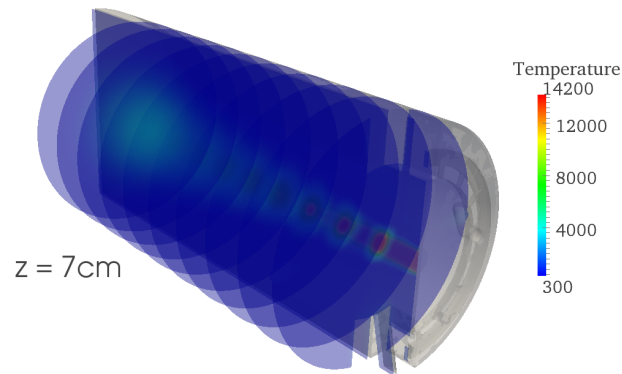


Figure 3.2: Planes to sample data from [5]

The results from the simulations done by University West were divided into a set of planes normal to the axial direction of the plasma jet, seen in *Figure 3.1*. All the sampled planes can be seen in *Figure 3.2*. With the aim of not having to include the different species in the simulations in this work a plane where the concentration of species were dominated by air was chosen to sample velocities and temperatures. Also, the temperature in the chosen plane should be low enough so that no chemical reactions such as ionization takes place downstream of the plane. The chosen plane is situated 70 mm downstream of the plasma inlet and the minimum concentration of air is 66%, which can be seen in *Figure 3.3*. The maximum temperature in each of the sampled planes is plotted in *Figure 3.4*.

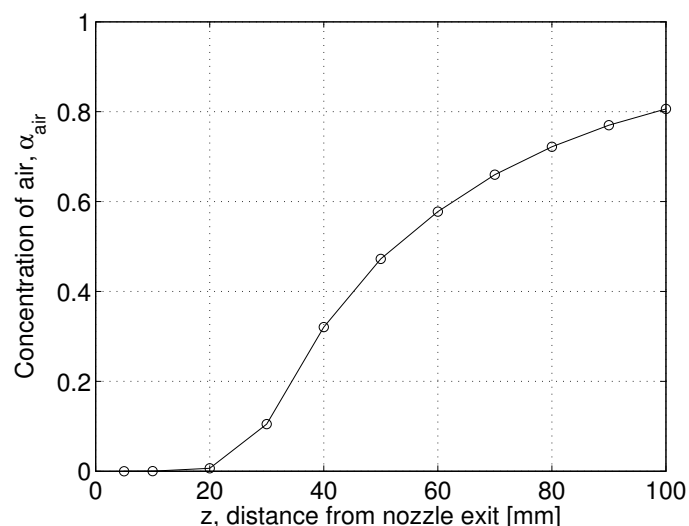


Figure 3.3: Minimum concentration of air along jet axis [5]

The data from the 70 mm downstream plane was stored and a pre processing tool was written in Matlab to sample velocities and temperatures from the plane, divide it into a set of injection zones, define an applicator and write it to a file that can be imported into

IBOFlow. In IPS Virtual Paint an applicator is defined through specifying axial, radial and tangential velocities, temperatures, volume flow of paint and standard deviations in a set of injection zones.

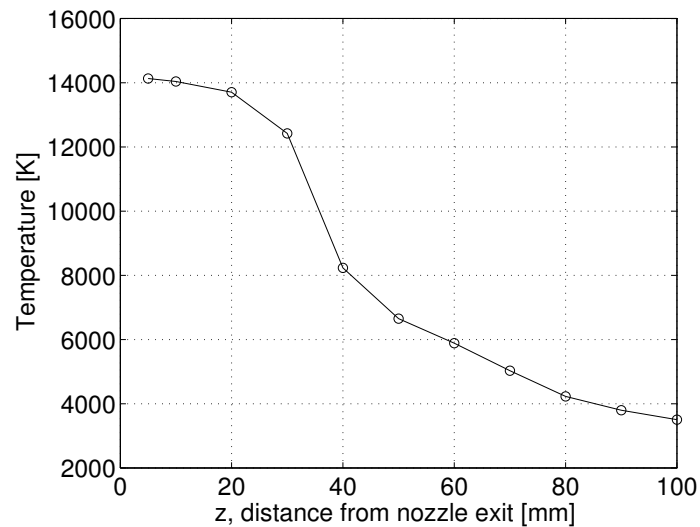


Figure 3.4: Maximum temperature in each plane along jet axis [5]

These properties were sampled in the chosen plane and exported as an .xml-file defining the applicator which was later imported into the solver (see *Section 3.2*). In *Figure 3.5* the data points from the chosen plane can be seen. The injection zones are defined within the black circles in the figure and in this case 6 injection zones were defined in the plane. The resulting data can be seen in *Table 3.1*.

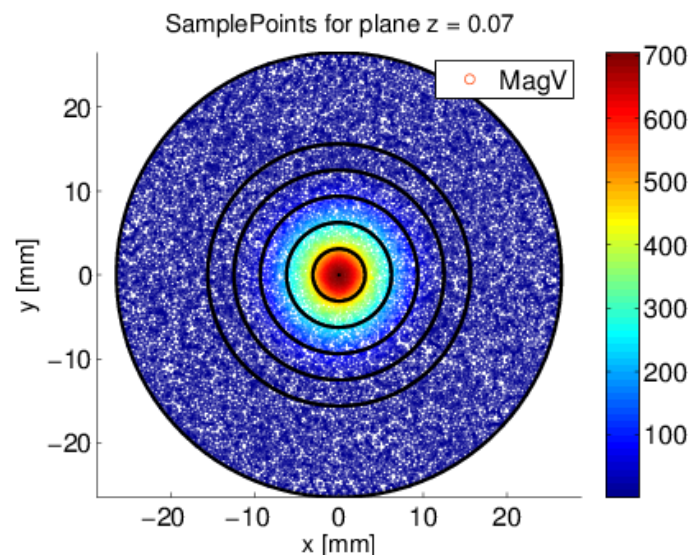


Figure 3.5: Sampled datapoints from plane $z = 70$ mm downstream of the plasma inlet

The radii of the injection zones should be chosen so that the standard deviations within each zone is minimized. The number of injection zones defined will determine how accurately the plasma gun is modeled and the limiting factor is the mesh resolution of the fluid solver, which has to be smaller than the smallest injection zone. The mean velocity in each polar coordinate direction, temperature and standard deviation of the velocity was calculated from the sampled data points in the plane, *Figure 3.5*, and is given in *Table 3.1*.

Air Injection zone 1		Air Injection zone 4	
R_{min}	0.0000 mm	R_{min}	9.3750 mm
R_{max}	3.1250 mm	R_{max}	12.500 mm
v_z	563.17 m/s	v_z	34.478 m/s
v_r	-0.3359 m/s	v_r	0.0323 m/s
v_φ	-2.7528 rad/s	v_φ	6.0982 rad/s
T	4425.9 K	T	1050.3 K
σ_v	0.1247	σ_v	0.5396

Air Injection zone 2		Air Injection zone 5	
R_{min}	3.1250 mm	R_{min}	12.500 mm
R_{max}	6.2500 mm	R_{max}	15.625 mm
v_z	374.49 m/s	v_z	2.7609 m/s
v_r	-0.2179 m/s	v_r	0.0220 m/s
v_φ	-95.596 rad/s	v_φ	2.5274 rad/s
T	3702.5 K	T	380.67 K
σ_v	0.2031	σ_v	0.8441

Air Injection zone 3		Air Injection zone 6	
R_{min}	6.2500 mm	R_{min}	15.625 mm
R_{max}	9.3750 mm	R_{max}	26.487 mm
v_z	139.98 m/s	v_z	0.0932 m/s
v_r	0.0606 m/s	v_r	0.0009 m/s
v_φ	5.8017 rad/s	v_φ	-0.0566 rad/s
T	2432.8 K	T	300.00 K
σ_v	0.3389	σ_v	0.0000

Table 3.1: Air injector settings

3.1.2 Defining the particle injector

In a real plasma gun the particles are injected into the plasma core, in- or outside the nozzle. In the reference case, *Appendix A*, the particles are injected perpendicular to the axial direction of the plasma jet. The air injector described above was however defined in a location downstream of this point. Therefore the particle injector has to be approximated by studying the particles properties in the sampled plane.

When setting up the particle injector the dispersion of particles due to plasma fluctuations were approximated by a adding a random factor to the particle velocity and direction, the standard deviation σ_v in *Table 3.2*. In [8] the particles' velocities along their mean trajectories are calculated and the powder has the same size as in the reference case in *Appendix A*. In the axial position $z = 70$ mm the particle velocities are approximately 200 m/s.

In an IPS Virtual paint applicator, an injection zone is either of injector type "paint" or "air". The former only injects particles and the latter only injects air. In each zone the axial, radial, and tangential velocity (v_z, v_r, v_φ) are specified. In *Section 3.1.1* the flow of paint was set to zero defining a pure air applicator. In the particle injector however, the flow of paint was specified according to *Appendix A*. Based on this information the particle injector brush was defined according to *Table 3.2*.

Particle injection zone	
R_{min}	0 mm
R_{max}	6 mm
v_z	200 m/s
v_r	0 m/s
v_φ	0 m/s
σ_v	0.1

Particle properties	
$r_{p,mean}$	67.5 μm
γ_r	0.1
ρ_p	7810

Table 3.2: Particle injector settings

3.2 Simulations

In 3.1 the plasma gun was defined. In this section the next step in the plasma spraying process is described, namely the fluid flow simulations and tracking of particles given the initial conditions.

3.2.1 Calculation domain

The domain is defined by specifying a geometrical lower bound of the simulation box, initial cellsize and number of cells in each cartesian direction. IBOFlow has a built-in meshing application that works on a set of refinement options to adapt the mesh for the specific simulation. The available refinement options are:

- Refine around Immersed Boundary (IB) (option 1)
 - Refines a specified number of times around the IB.
- Refine box (option 2)
 - Refines a specified number of times in a box specified by lower and upper bounds.
- Refine around applicator (option 3)
 - Refines a specified number of times around the applicator.
- Automatic grid update (option 4)
 - Boolean function, true allows IBOFlow to update the mesh as the IB:s and applicators move.
- Refine Error (option 5)
 - Boolean function, refines the cells where the largest relative errors appear.

In both test cases the "automatic grid update" option was used since the applicator is not static. When using the option that refines around the IB:s, option 1, the mesh is refined in all directions normal to the surface of the IB. In the case of the plate it was only interesting to resolve the flow between the plate and the applicator and hence a box-refinement, option 2, on the top surface of the plate was used.

In *Figures 3.6, 3.7 and 3.8* the domain is visualized. The number of refinement levels around the plate is 6. The cell size of all positions has only one degree of freedom according to *Equation 3.1*:

$$\Delta x_N = \frac{\Delta x_{initial}}{2^N} \quad (3.1)$$

where N is the number of refinements. In this case, the initial cell size was $\Delta x_{initial} = 0.1$ m which gives $\Delta x = 1.5625$ mm close to the plate.

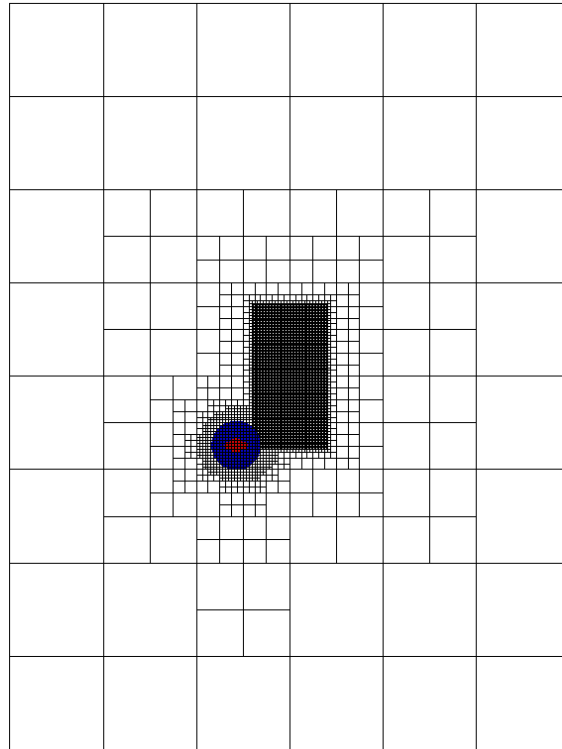


Figure 3.6: Calculation domain, $x - y$ plane. Refined around plate and applicator

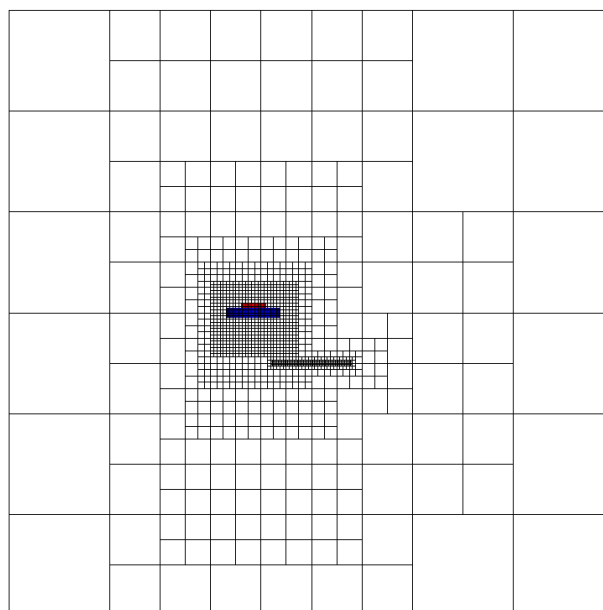


Figure 3.7: Calculation domain, $x - z$ plane

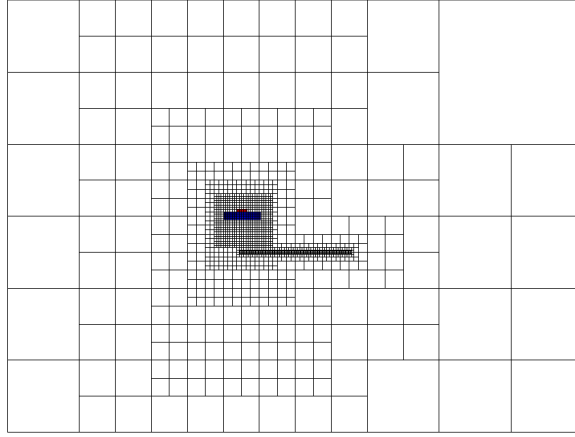


Figure 3.8: Calculation domain, $y - z$ plane

In *Figures 3.6 to 3.8* the plate is located in the middle of the domain. The applicator is in its starting position and the refinements around both target and applicator are seen.

As stated in *Section 3.1.1* the grid resolution close to the applicator must be at least as fine as the thinnest injection zone to resolve the applicators radial velocity gradient. Thus the constraint of *Equation 3.2* is implied

$$\Delta x \leq (R_{outer} - R_{inner})_{injectionZone} \quad (3.2)$$

As the plasma gun moves over the plate the refinement will adapt so that the cells close to the applicator is always refined 5 levels ($\Delta x = \Delta x_{init}/2^5 = 3.125mm$). If a static grid was used the whole area covered by the applicator movement would have to be refined 5 levels.

3.2.2 Boundary Conditions

Boundary conditions are specified on the faces of the domain, and the choices of boundary conditions are listed in *Table 3.3*. Also, thermal boundary conditions must be specified. The options of thermal boundary conditions are listed in *Table 3.4*

Boundary Conditions	Definition
Inlet	Velocity Dirichlet
Inlet Pressure	Velocity and pressure Dirichlet
Outlet	Pressure Dirichlet
Wall	Dirichlet velocity = 0
Wall Function	Wall with flat plate boundary layer
Symmetry	Neumann for velocity and pressure, no mass flux through boundary
Free	Neumann for velocity and pressure, mass flux through boundary can be present

Table 3.3: Boundary conditions in IBOFlow

Thermal Boundary Conditions	Definition
Inlet	Dirichlet temperature
Wall	Dirichlet temperature, no convection
Symmetry	Neumann, no temperature gradient over boundary

Table 3.4: Thermal Boundary conditions in IBOFlow

The boundary conditions used in the simulations of this work are given in *Table 3.5*. They are applied to the boundaries of the domain seen in *Figures 3.6 to 3.8*. The top boundary of the domain is given an inlet velocity of 1 m/s into the domain which stabilizes the flow in the sense that the fluid which flows over the edges of the plate will be turned towards the bottom boundary where the outlet is located. Also, one of the main differences between the modeled process and the real one is that mass is added by the plasma gun in the real process but in the simulations no mass is added. Instead a volumetric force is applied to the cells located at the position of the plasma gun that accelerates the flow to the correct velocity in this region.

Face	Normal	Boundary condition	Thermal
East	X	Symmetry	Symmetry
West	-X	Symmetry	Symmetry
North	Y	Symmetry	Symmetry
South	-Y	Symmetry	Symmetry
Top	Z	Inlet ($v_z = -1.0$ m/s)	Wall
Bottom	-Z	Outlet ($p = 0.0$ Pa)	Symmetry

Table 3.5: Thermal Boundary conditions in IBOFlow

Also, the treatment of the immersed boundary is specified. There are several different immersed boundary methods and a thorough description can be found in [15]. *Table 3.6* lists the available immersed boundary options. In all simulations included in this work, the mirroring immersed boundary method has been used.

IB Method	Definition
First order method	Distributive method, if the cell centre is inside the IB a Dirichlet conditions is set. This will create a step-interface between fluid and IB.
Mirror	Mirrors the velocityfield over the normal of the immersed boundary
Hybrid	Hybrid Extrapolation/Mirroring immersed boundary method. The extrapolation creates a wall function from the cell-centre closest to the IB (point 1), a fictive point outside the previous point (point 2), and the point on the IB

Table 3.6: Immersed boundary methods

3.3 Solver settings

In this section the settings for solving the governing equations are described. It includes convective scheme, time-discretization and fluid solver type.

The options and short descriptions of the available convective schemes are given in [Table 3.7](#). Statements of accuracy refer to the Taylor series truncation error, defined in [\[23\]](#).

Convective Scheme	Definition
First order upwind	Face velocity $v_f =$ upwind cell-center velocity v_U , conservative, bounded, transportive, first order accurate scheme.
First order downwind	$v_f =$ downwind cell-center velocity v_D , same properties as first order upwind.
Second order upwind	v_f is calculated from two upwind cell-centers, second order accurate.
Central differencing	$v_f = \frac{1}{2}(v_P + v_{Neighbour})$ for equidistant mesh. The cellface velocity is always interpolated from the two closest cell-centers.
Lax Wendroff	Upwind for large face CFL numbers and central scheme for low local courant numbers.
Hybrid	Combination of central differencing and Upwind. Upwind in convection-dominated regions and central differencing in diffusion-dominated regions.

Table 3.7: Convective schemes in IBOFlow

The Courant Friedrichs Lewy (CFL) number is defined as $CFL = \frac{u\Delta t}{\Delta x}$. The cell size close to the applicator is $\Delta x = 3.125$ mm. The explicit time discretization is conditionally stable with an upper limit of the CFL-number ($CFL \leq 1$) which, remembering that the largest velocity in the air injector is 565 m/s, [Table 3.1](#), would limit the timestep to 5.5 μ s. A real plasma spraying process has a timespan of several seconds or perhaps minutes, hence the explicit time scheme would be very computationally demanding.

The implicit time discretization is however unconditionally stable and the CFL-numbers can be larger than one. However the accuracy is decreased as the CFL-number is increased. The time schemes available in IBOFlow are listed in [Table 3.8](#)

Time Scheme	Definition
Implicit Euler	All solution variables in the discretization are evaluated at time $t = n + 1$, hence a system of equations have to be solved.
Explicit Euler	All solution variables in the discretization are evaluated at time $t = n$, the solution is explicitly given by the previous solution, this scheme is first order accurate.
Crank-Nicolson	Contributions of solution variables at time $t = n$ and $t = n + 1$ are used to calculate the solution ($f = 1/2$ in <i>Equation 2.8</i>). A system of equations has to be solved, the scheme is second order accurate.

Table 3.8: Convective schemes in IBOFlow

3.4 Postprocessing

The simulations of *Section 3.2* results in a set of particle impacts, the information in the output is the coordinates, volume and time of impact for each particle. In this section a post processing tool that has been developed is described. The purpose of the tool is to predict the heat transfer from the impacting particles through the coating and target. The tool has not been used to produce any results regarding residual stresses in the target or predictions of bonding strengths in the coating. It is purely developed to be an indication of what can be done in the future.

3.4.1 splashHeat3D

The aim of this post processing tool is to predict how the heat is conducted through the coating and into the sprayed target. The implementation is based on the theory of *Section 2.6*.

The particles in the reference case in *Appendix A* consist of Nickel with 5wt% Al. The properties of Ni and Al are given in *Table 3.9* and the assumption has been made that the particles are fully liquid at the point of impact. Thus, no part of the particles will be solid nor vaporized which gives the particle temperature range $T_{Ni,melt} < T_{particle} < T_{Al,vap}$. Since the density of Ni is considerably higher than the density of Al, the volume fraction and weight fraction are not equal. In *Table 3.9* the properties of the coating have been calculated for the volume fraction of Al and Ni, respectively. This way of calculating the coating properties are perhaps not very realistic since several metallurgic processes and oxidation are taking place. Hence, before using this theory on practical problems the real coating characteristics should be measured or calculated in a different way.

	Ni	Al	Coating
vol%	83	17	—
ρ	8900	2700	7841
C_p	540	902	610
k	91	237	116
T_{melt}	1728	933	1728
T_{vap}	3186	2792	2792

Table 3.9: Properties of coating

These coating properties are used to calculate the coefficients in the finite volume code described in *Section 5.3*.

The calculation domain consists of cells above the surface of the target and cells below the surface of the target. Initially, cells above the surface will contain air and thus have the transport properties of air. As spray particles impact on the surface the cells above the surface will gradually be filled with coating and hence the transport coefficients will change to the coating properties of *Table 3.9*. The transport properties of each cell must therefore be updated every time a particle impacts the cell and increases the volume fraction of coating. The volume fraction is defined in as

$$\alpha = \frac{V_c}{\Delta V} \quad 0 \leq \alpha \leq 1 \quad (3.3)$$

In *Equation 3.3*, V_c is the volume of coating in the cell and ΔV is the cell volume. The transport properties of the cell are then calculated as:

$$\Phi_{cell} = \alpha\Phi_{coating} + (1 - \alpha)\Phi_{air} \quad (3.4)$$

where Φ is any property of the coating. In *Figure 3.9* the calculation domain is displayed together with the plate used in the IBOFlow-simulation.

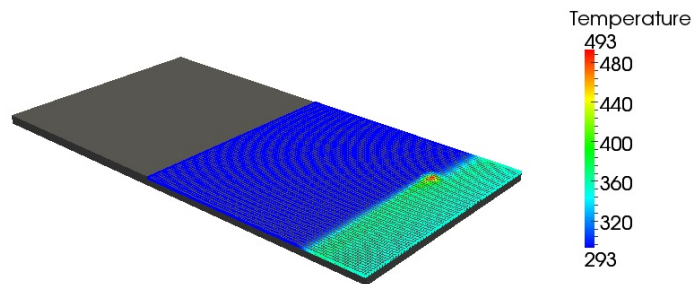


Figure 3.9: Heat transfer calculation of test case 1

4 Physical Testing

The tested process is *Plasma Spraying* and two test cases were defined according to *Section 1.4*. The aim of test case 1 and 2 was to compare thickness profiles (testCase1) and to visually inspect the appearance of individual sweeps (testCase2). The gun velocity was 1.25 m/s and the spraying distance was 120 mm for all tests. Also, a third test case was performed. However the results did not contribute with any further information and have therefore been omitted from this report. It is instead included in *Appendix C*.

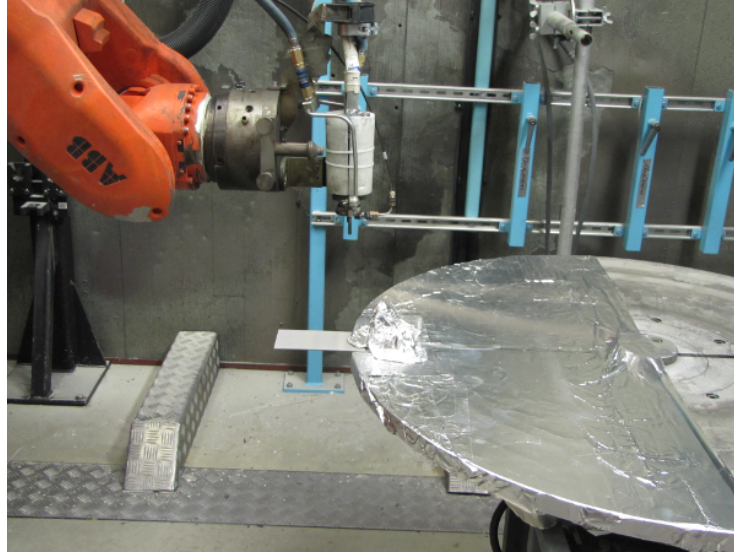


Figure 4.1: Setup, plasma gun disabled

The setup of the tests is presented in *Figures 4.1* and *4.2*. The target plate is secured to the table and the plasma gun is attached to a robot arm. The robot arm was programmed so that the plasma gun follows the path specified by *Figures 1.1* and *1.2*. In test case 1, each step is 3.5 mm and each sweep is 115 mm.

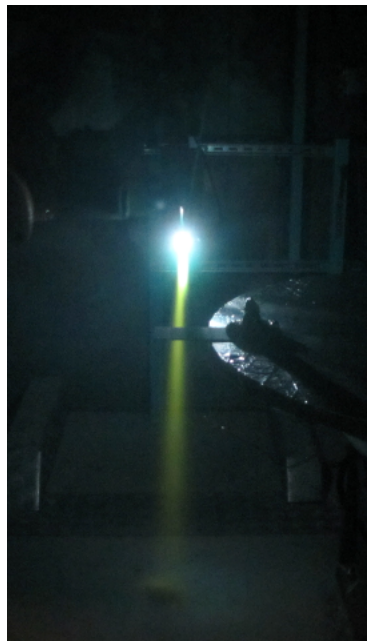


Figure 4.2: Setup, plasma gun active

The powder particles consist of Ni-5wt%Al and the mean radius is $33.75 \mu\text{m}$. The particle velocities and temperatures were measured along a line perpendicular to the axis of the plasma jet, namely at two points 70 and 120 mm downstream of the plasma nozzle exit. The particle temperatures are approximately 2400 K and the particle velocities are approximately 200 m/s at the center of the measured line in the first measurement position. In the second position the particle temperature had increased to 2800 K and the velocities had decreased to 155 m/s. Hence the fluid temperature in the region between the two measurement points must be greater than the particle temperature. The particles are decelerated between the two positions and thus the particle velocity is larger than the fluid velocity in this region.

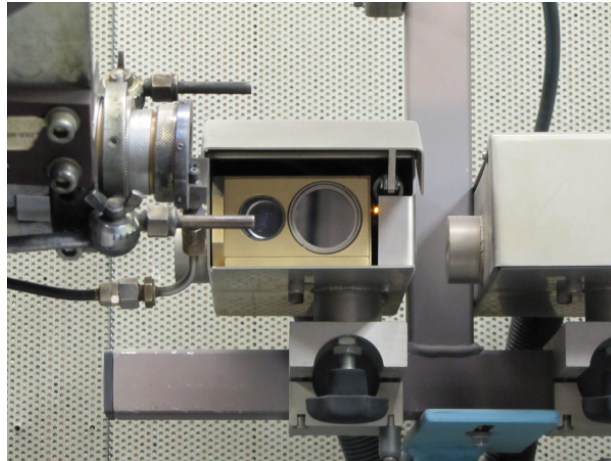


Figure 4.3: Measurement position, plasma gun disabled

The measurements of particle velocity and temperature were performed when the plasma gun was in the measurement position seen in *Figures 4.3* and *4.4*. The measurement device is described by Choquet et al. in [5]



Figure 4.4: Measurement position, plasma gun activated

Below the results from the physical testing are given.

4.1 Test Case 1

In *Figures 4.5* and *4.6* the results from test case 1 are presented. The measured coating thickness was 50-60 μm for 4 cycles (measured with a micrometer). Hence, every cycle should contribute with approximately 12.5 - 15 μm . Note that color enhancement has been used in the pictures for better visualization; this applies for all images of sprayed plates.

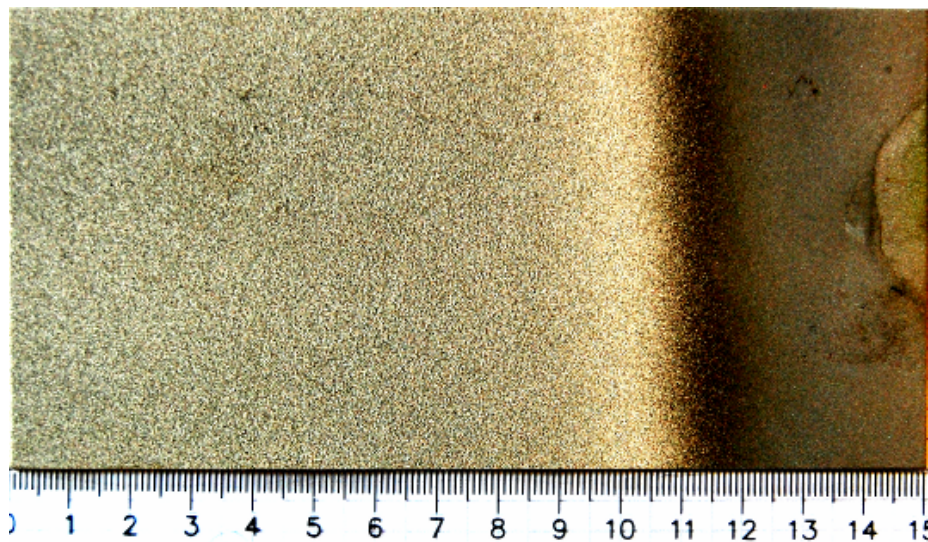


Figure 4.5: Result, test case 1, first target

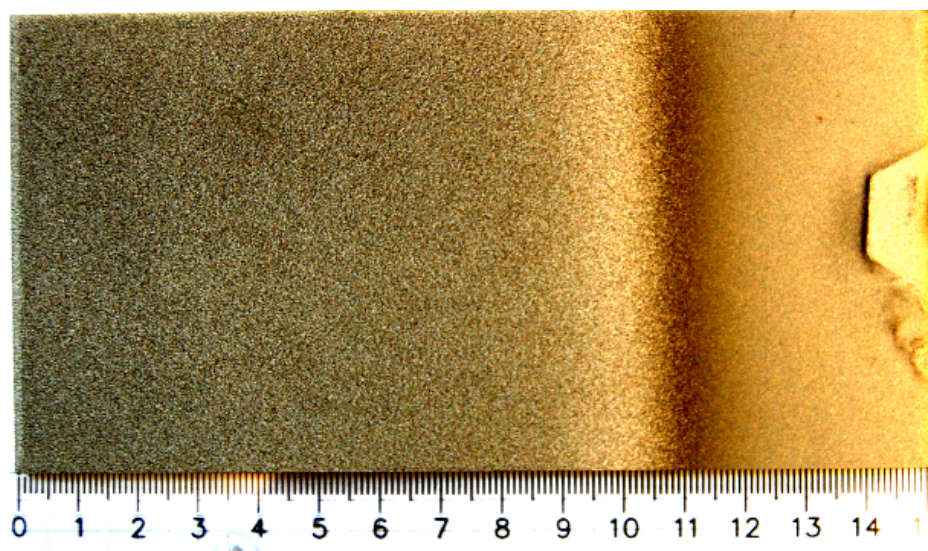


Figure 4.6: Result, test case 1, second target

4.2 Test Case 2

The results of test case 2 are presented in *Figures 4.7* and *4.8*. The hypothesis prior to testing was that the sweep width would be greater when the particles were injected perpendicular to the gun movement compared to aligned with the gun movement. However, the tests proved the opposite.

In *Figures 4.7* and *4.8* the gun started at the top right, swept across the plate, moved 60 mm to the left, rotated 90° and then swept to the top left (as described in *Figure 1.2*)

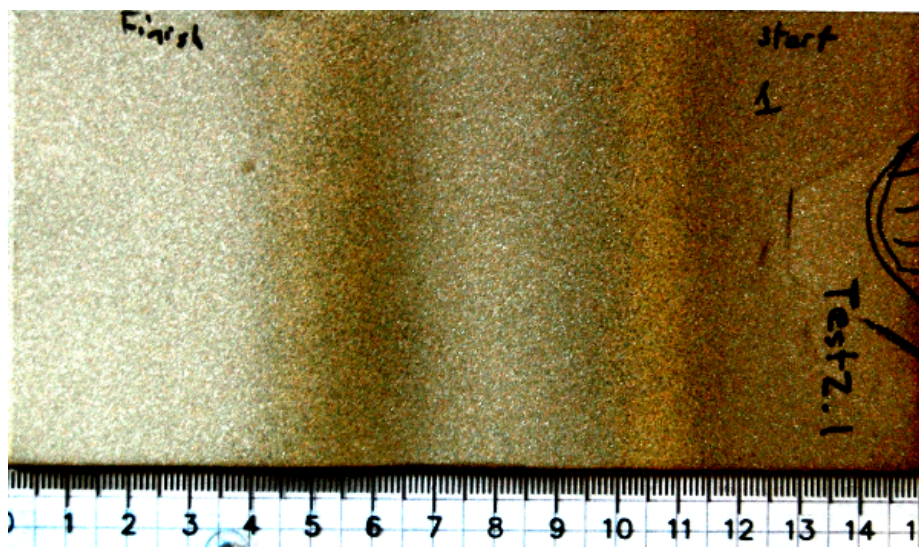


Figure 4.7: Result, test case 2, first target

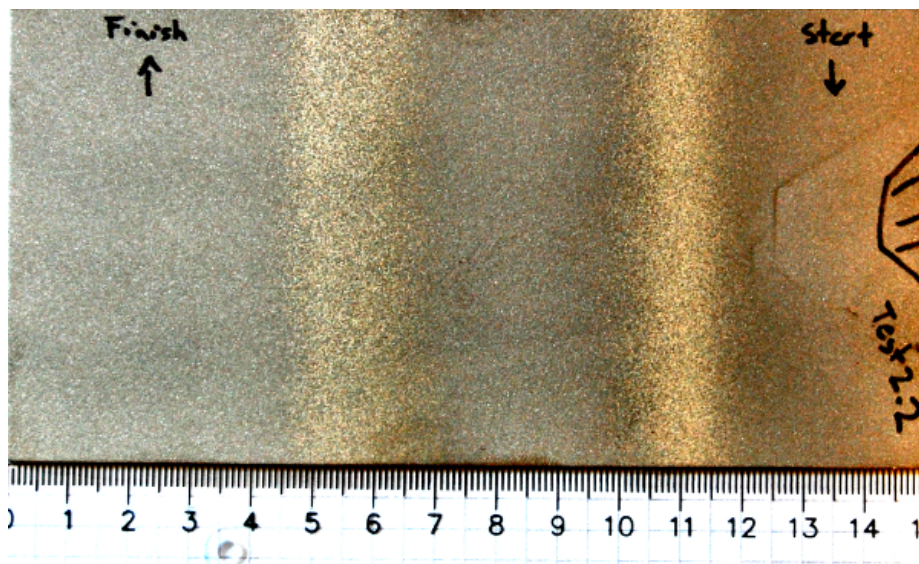


Figure 4.8: Result, test case 2, second target

The width of the first sweep is approximately 15 mm and the width of the second sweep is approximately 25 mm. Thus, the difference between sweeps is quite clear.

5 Results

As stated in *Section 4* the physical testing showed that the particle velocities had decreased between the measurement points 70 and 120 mm downstream of the plasma nozzle exit which indicates that the particles have a higher velocity than the fluid in this region. The fluid velocity was not measured during testing and therefore the maximum inlet velocity in the air injector was set to 200 m/s and the particles were injected with the same velocity in the simulations. The air applicator defined in *Section 3.1*, that was based on temperature dependent indata, was modified to make the particles behave as in the physical testing.

The reason for the modification is that the simulations where the temperature dependence was included were unstable due to the weak coupling of equations. The density and viscosity used in the Navier-Stokes solver of IBOFlow were based on the old temperature and hence explicitly given. See *Section 7* for a suggestion of how to solve this problem.

In *Figure 5.1* the fluid flow is visualized, and in *Figure 5.2* the particles' trajectories are presented. Note the vertical lines in *Figure 5.2* indicate the different types of injectors. The dark blue line represents the air-injector and the remaining are particle injectors. The right- and leftmost injector set represent the start and end position of the applicator movement for the sweep.

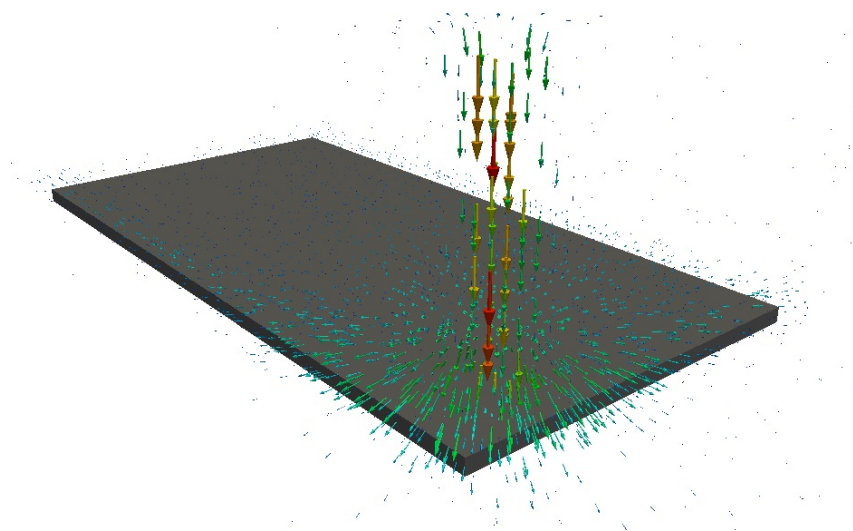


Figure 5.1: Velocity vectors of the fluid flow

The results are presented for each of the two test cases defined in *Section 1.4*. The two test cases have also been tested in a real plasma spraying process at Volvo Aero and the results from the physical testing is used to calibrate and validate the model. In general, a good agreement with the tests have been achieved.

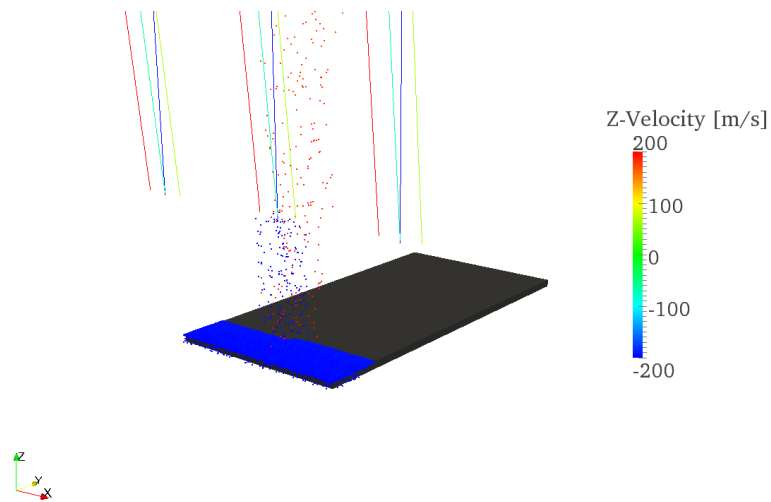


Figure 5.2: Particles injected in the flow. Three particle injectors and one air injector

5.1 Test Case 1

The results from the IBOFlow simulations are given for four different reflection settings between 30 and 50%. The reflection determines how much of the particles that do not stick to the target upon impact. *Figures 5.3 to 5.6* show the thickness profile of test case 1.

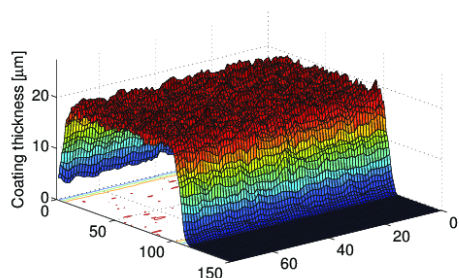


Figure 5.3: 30% reflection

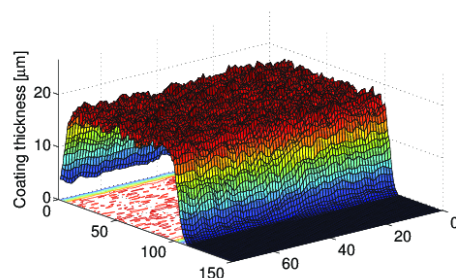


Figure 5.4: 35% reflection

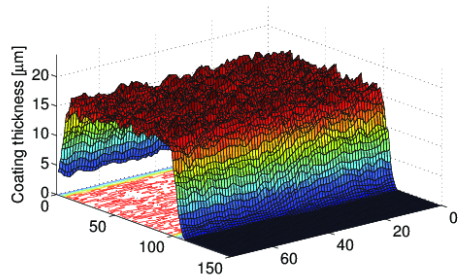


Figure 5.5: 40% reflection

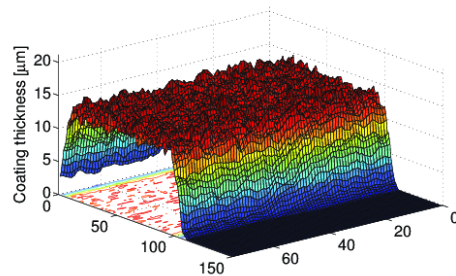


Figure 5.6: 50% reflection

In *Figure 5.7* the mean thickness for 30, 35, 40 and 50% reflection is given. Note that only one cycle has been simulated, i.e. the thickness should be one fourth of the thickness of the physical tests.

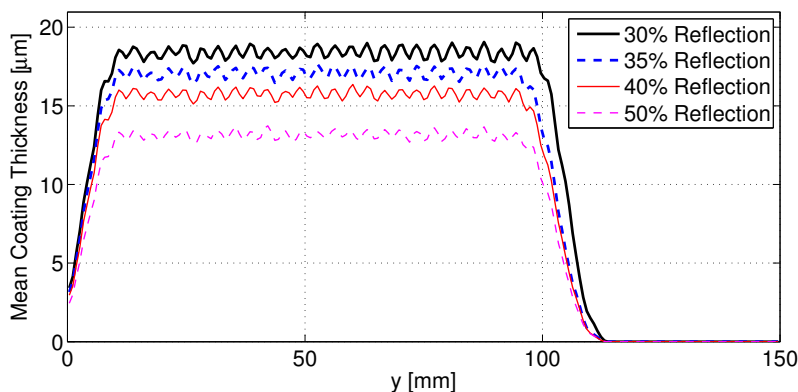


Figure 5.7: Mean thickness along the plate, Test Case 1

In the case of 50% reflection the thickness is approximately $12.5 \mu\text{m}$ which corresponds to $50 \mu\text{m}$ for four cycles. Hence, 40-50% of the particles are reflected. The simulation time for one cycle of 29 sweeps is approximately 25 h.

5.2 Test Case 2

5.2.1 Simulations

The simulations of test case 2 have been performed for three different settings of reflection. The goal has been to fine tune the settings for the applicators, reflections and velocities so that the results agree with the physical tests.

After performing the tests it was found that the originally designed virtual applicator of *Section 3.1.2* did not produce the desired results, hence a redesign was forced. The reason for this was that the original hypothesis was that the sweeps would be wider whilst the particles were injected perpendicular to the gun movement. Tests showed the opposite and it was realized that the plasma jet must flatten the column of injected particles into an oval shape. Therefore, an oval particle injector was designed by combining circular injection zones as can be seen in *Figure 5.8*

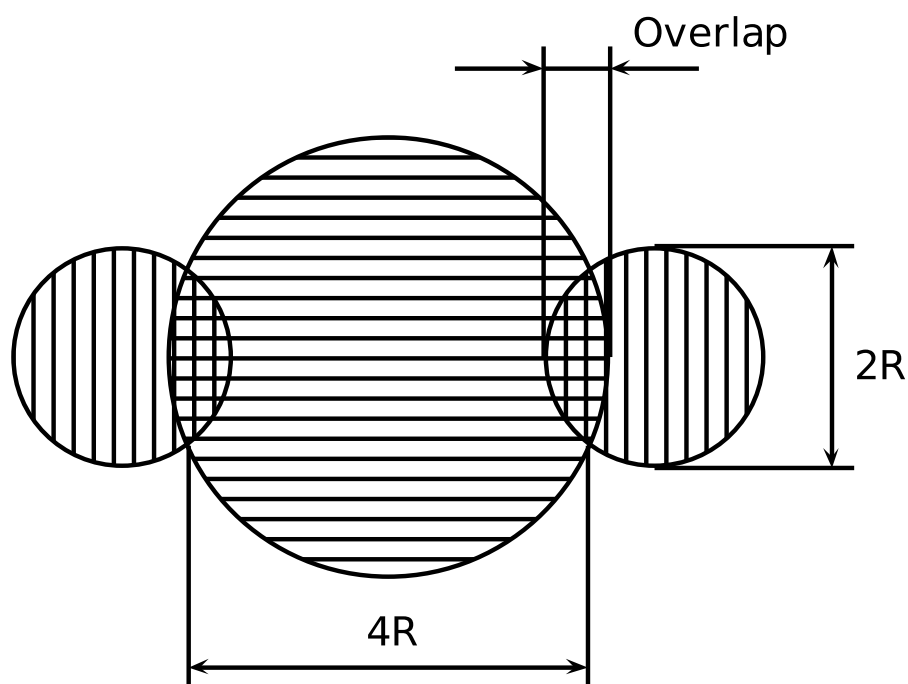


Figure 5.8: The oval particle injector

The parameter R was set to 3.75 mm so that $4R$ matches the width of the sweeps (15 mm). The overlap was set to 2.5 mm so that $4R - \text{Overlap} = 12.5$ mm (width of sweeps with particle injection aligned with gun movement).

With this particle injector the following results were retrieved; *Figure 5.9* show the thickness for 30% reflection and *Figure 5.10* show the mean thickness for all y bins.

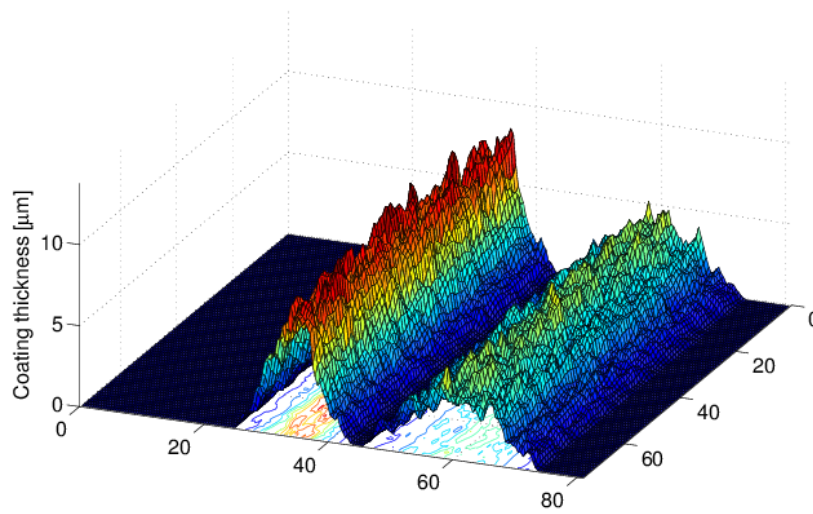


Figure 5.9: 30% reflection, Coating Thickness

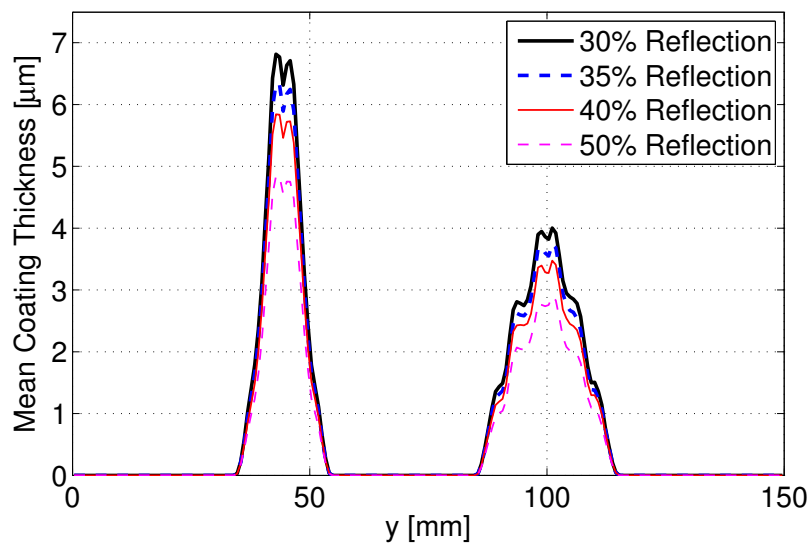


Figure 5.10: Mean Coating Thickness for different reflections

5.2.2 Comparison

In *Figure 5.11* a comparison between the physical testing and simulations is shown.

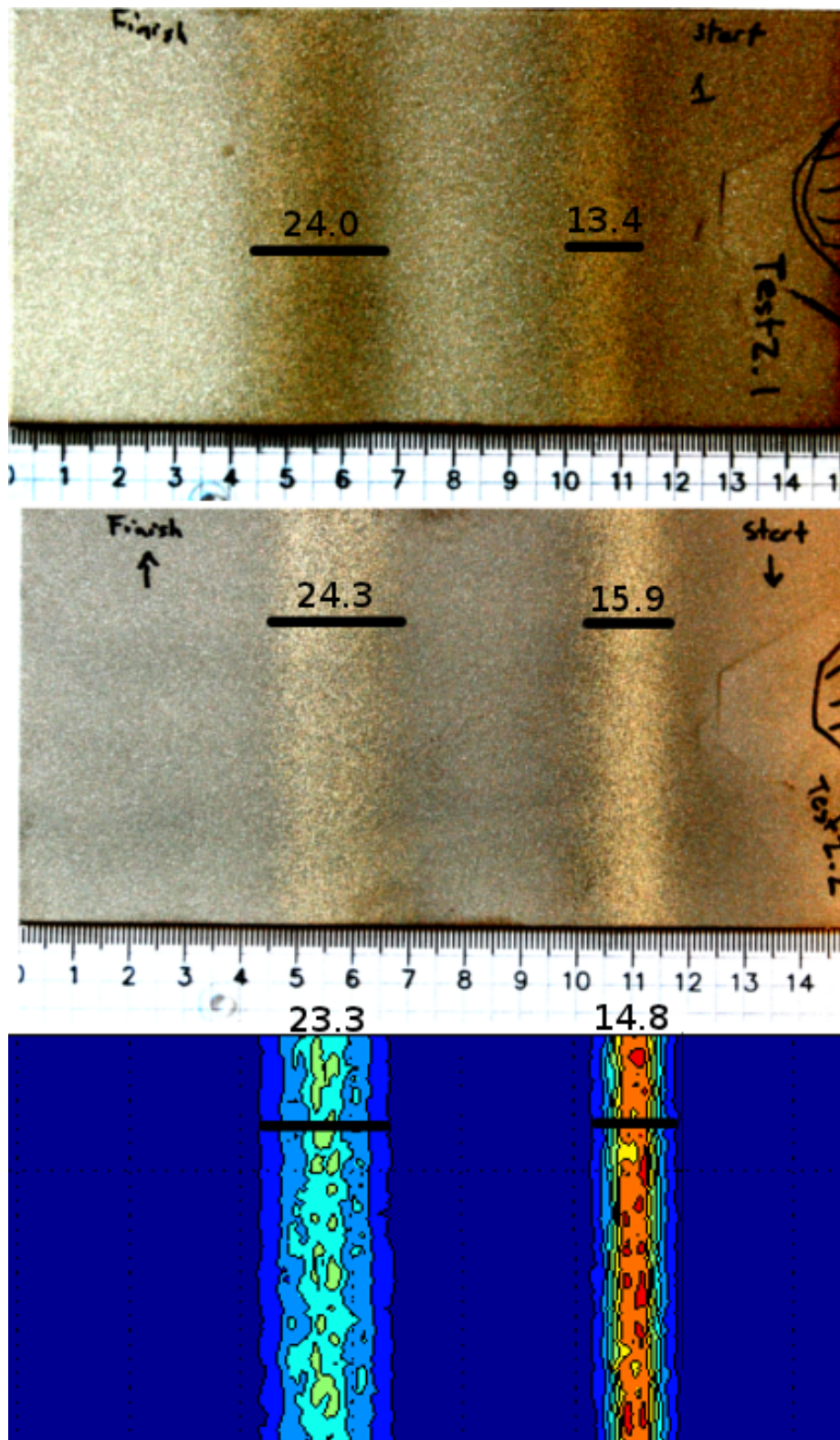


Figure 5.11: Measurements of physical tests and simulations.

5.3 Coating heat transfer solver

The development of this structured grid finite volume heat transfer solver was done in Matlab [17]. The theory of *Section 2.6* has been implemented and validated against the analytical solution of *Appendix B*.

A validation case in two dimensions was set up where a hat function with $T = T_0$ in the center of the domain was used to initialize the field. Dirichlet boundary conditions, $T = 0$, are used for all boundaries.

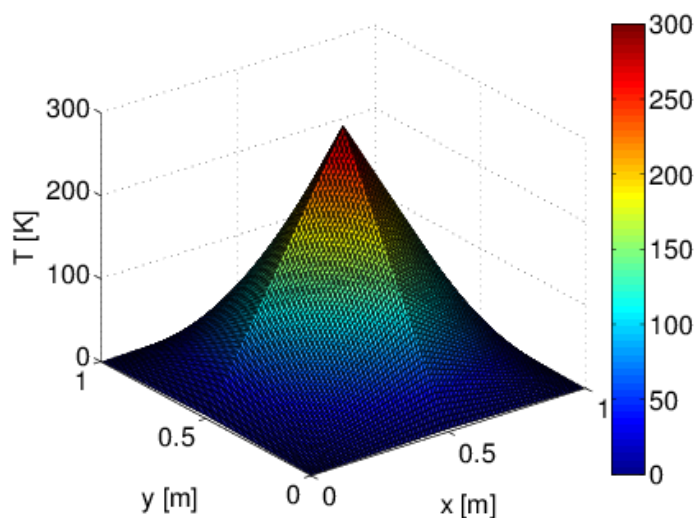


Figure 5.12: Initial conditions

The analytical solution is derived in *Appendix B* and is given by *Equation 5.1*. The initial condition is visualized in *Figure 5.12* and the solution after 120s is visualized in *Figure 5.13*.

$$T(x, y, t) = \sum_{n=1}^{\infty} \sum_{m=1}^{\infty} \beta_{n,m} \sin\left(\frac{n\pi}{L}x\right) \sin\left(\frac{m\pi}{H}y\right) e^{-\kappa\left(\left(\frac{n\pi}{L}\right)^2 + \left(\frac{m\pi}{H}\right)^2\right)t} \quad (5.1)$$

$$\beta_{n,m} = T_0 \frac{64}{n^2 m^2 \pi^4} \sin\left(\frac{n\pi}{2}\right) \sin\left(\frac{m\pi}{2}\right)$$

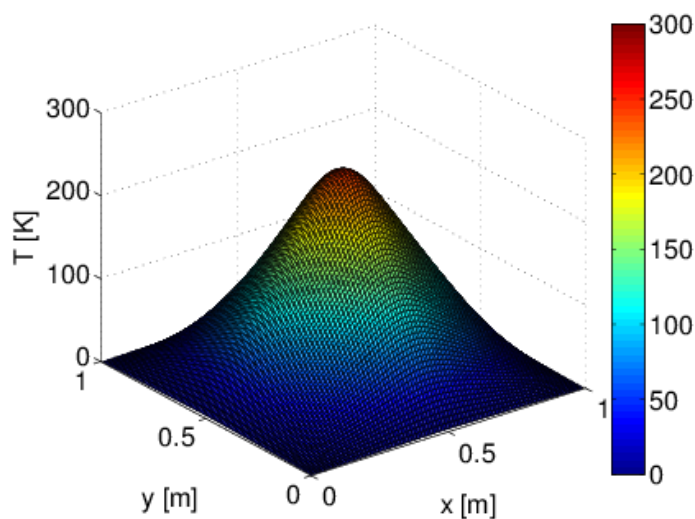


Figure 5.13: Temperature after 120 s.

A grid study was performed to determine the convergence of the models spatial resolution. Theory states that the error, which is defined in *Equation 5.2*, should be proportional to the cell size squared. A timestep of $\Delta t = 10^{-3}$ s was used when comparing the different meshes.

$$err_N(t) = \frac{\|T_N^{numerical}(t) - T^{analytical}(t)\|_2}{\|T^{analytical}(t)\|_2} \quad (5.2)$$

where N is the number of cells in the respective directions and $\|T\|_2$ is the Euclidean norm of T . Hence, if the model is correct, $err_N(t_{end}) \propto \frac{1}{N^2}$. In *Figure 5.14* the solution is plotted at $y = 0.5$ after 120 s for the 1×1 m thin plate. The error after 120 s for 7 different meshes is plotted in *Figure 5.15*.

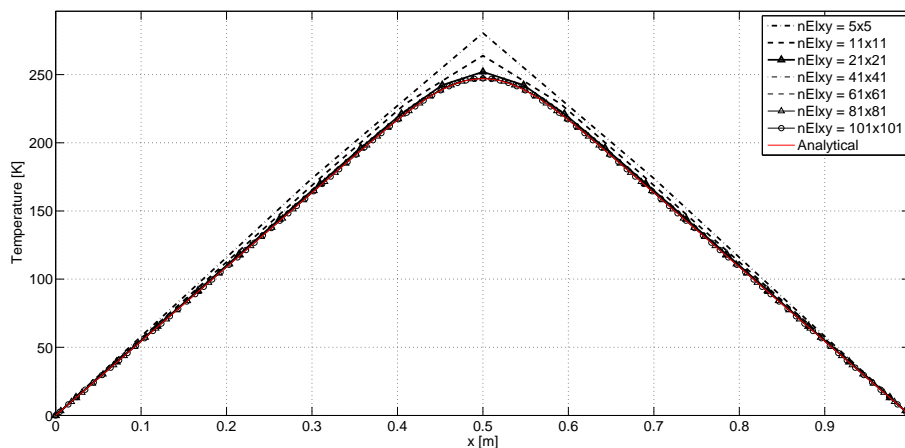


Figure 5.14: Solution for different meshes after 120 s.

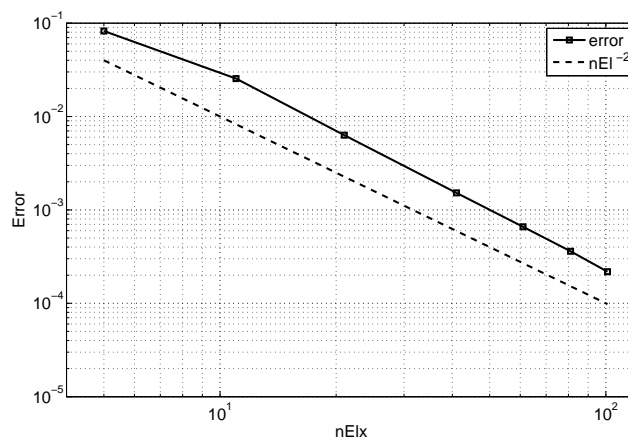


Figure 5.15: Error for different meshes after 120 s

The second order convergence is confirmed in *Figure 5.15*. In *Table 5.1* the error is given in numerical values, and it can be seen that it is in the order of 10^{-4} for the finest mesh.

N	$err_N(t = 120)$
5	8.2466e-02
11	2.5488e-02
21	6.3194e-03
41	1.5224e-03
61	6.5938e-04
81	3.6083e-04
101	2.1787e-04

Table 5.1: Endtime error for different meshes

Also, a study of the timestep was made. The finest mesh was used to compare timesteps and the error is still defined according to *Equation 5.2*. The numerical and analytical solution after 120 s is plotted in *Figure 5.16* and the error after 120 s is plotted in *Figure 5.2*.

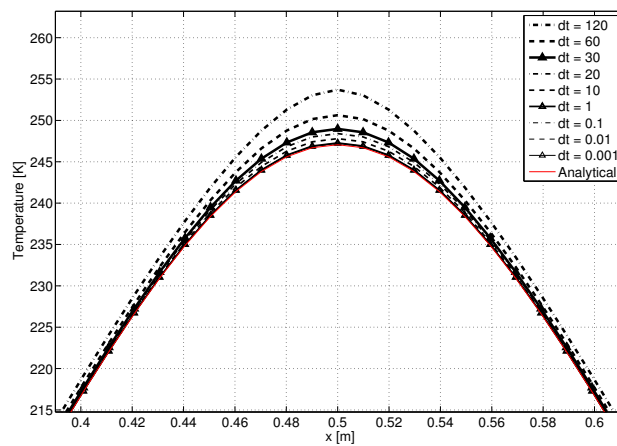


Figure 5.16: Solution for different timesteps after 120 s

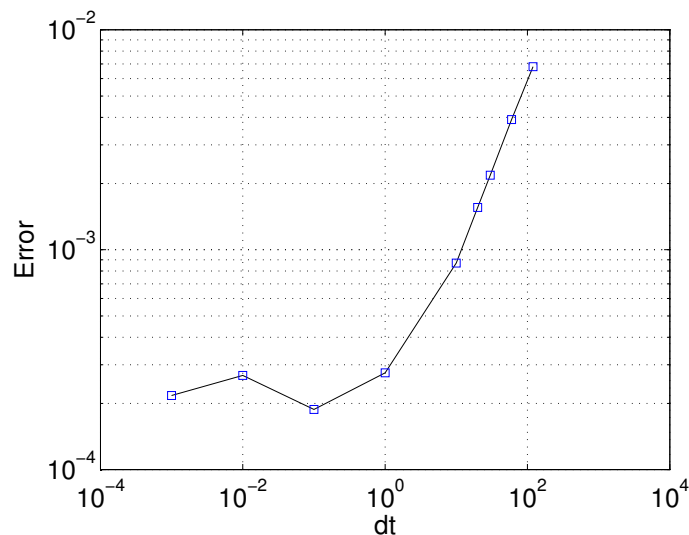


Figure 5.17: Error for different timesteps after 120 s

In *Figure 5.17* it can be seen that for timesteps $\Delta t \lesssim 1$ the spatial error is dominating. The numerical values are given in *Table 5.2*

dt	$err_N(t = 120)$
1.2e+02	6.7981e-03
6.0e+01	3.9095e-03
3.0e+01	2.1834e-03
2.0e+01	1.5574e-03
1.0e+01	8.6924e-04
1.0e+00	2.7579e-04
1.0e-01	1.8781e-04
1.0e-02	2.6839e-04
1.0e-03	2.1787e-04

Table 5.2: Endtime error for different meshes

6 Summary and Conclusions

The stated purpose of this work was to evaluate the possibilities of simulating thermal spraying using the software IPS Virtual Paint. Several simulations have been performed with results that are comparable to the results of the physical testing. This work has in addition developed a method to avoid the extreme computational times that simulating the whole plasma spraying process would require. This was accomplished by use of existing results of detailed simulations of the plasma flow and a developed method of merging the data to the setup of IBOFlow, the fluid flow solver of IPS Virtual Paint.

6.1 Input data

The indata to the simulations were built up by sampling data from existing simulations of the plasma jet and its close surroundings. These simulations were performed by University West and are described in [5]. The flow in the indata simulations were assumed turbulent. In this work the indata were imported into the visualization software *Paraview* where data from a set of planes, normal to the axis of the plasma jet, were extracted. A script in *Matlab* was written to read the data in the planes and divide each plane into a set of circular injection zones centered in the core of the plasma jet. The mean radial, tangential, and axial velocity, the mean temperature and the standard deviation of the velocity were then calculated for each injection zone and written to an .xml-file defining the applicator.

This is a simple and straight-forward method of extracting information from previously simulated plasma flow and it only needs to be done once per process since the flow upstream of the sampled plane is assumed to be constant. The physical testing also showed that the assumption of a steady plasma flow is quite valid since there are no visual fluctuations of the plasma jet upstream of the sampled plane.

The main loss of information when using this method is the particle-trajectories upstream of the sampled plane. In the reference case (*Appendix A*) the particles are injected in a 90°-angle into the plasma core 5mm outside of the plasma nozzle exit and accelerated towards the target. In this work the particles are injected in the plane of the applicator and the information of injection velocities and size of injection zones are based on the literature and physical testing.

6.2 Simulations

The literature was used to slightly adapt IBOFlow to take into account the temperature dependence of the transport coefficients in the momentum and energy equations. However, the temperature dependent properties made the simulations unstable and further development needs to be done to increase stability (see *Section 7*).

Simulations were performed on two test cases, the first to compare thickness profiles for several layers of spray and the second to compare individual sweeps. A model was set up with a few vital parameters to decide. The parameters include particle reflection fraction, width and angle of particle injector.

The particle reflection was not explicitly measured but by comparing thickness profiles of simulations and physical tests it was realized that the particle reflection fraction is approximately 50%. The physical tests showed that the sweeps where the particles are injected perpendicular to the gun movement are 40% thinner than when the particles are injected aligned with the gun movement. This is a significant difference and it proves that the particle column is not circular. To model the non-circular particle column an oval particle injector was introduced in which three circular injection zones of different radii were used. The radius of the large injection zone in the middle of the oval was specified so that the width of sweeps with perpendicular particle injection was achieved. The two smaller particle injection zones were given half the radius of the large, and the distance between the centers of the zones defined the other axis of the oval. A visualization can be seen in *Figure 5.8*.

Due to the lack of convergence in the temperature dependent simulations the particle temperature history could not be traced. The physical testing showed that the surface temperature of the particles at the spray distance 120 mm is approximately 3100 K and this should be used as input for the coating heat transfer solver.

6.3 Physical Testing

Physical testing was performed at Volvo Aero on three test cases, two of which have been compared to the simulations. In the third test case a curved sweep was sprayed to get information of the sweep width with particles injected 0° - 90° relative to the gun movement. However the plate was too small for this test so the radius of the curve was too small to retrieve any information. Hence it did not provide any additional information and was thus omitted from the results of this work. They are instead appended for the sake of completeness. If this test is to be repeated, larger target plates should be used.

The first test was performed to gain knowledge of the thickness of sprayed details. The simulation parameter to decide was the particle reflection fraction and it was found that approximately 50% of the particles are reflected. This result was found by comparing the thicknesses of the tests with the thicknesses of simulations with different settings of the particle reflection fraction. Ideally one would measure the exact amount of particle reflection, suggestions are given in *Section 7*.

7 Future Work

In this section a list of suggested future work is given.

- All simulations were performed in the Linux interface of IBOFlow. For the model to be industrially applicable the setup should be integrated into the graphical user interface of IPS Virtual Paint. In the GUI it is much easier to import general geometries and set up the calculation domain which is key for an efficient software tool. Generally, more simulations on more complex geometries should be performed.
- As stated in *Section 6* the temperature dependence of the fluid properties caused instabilities in the simulations. To correctly model the forces acting on each particle the temperature dependence of ρ and μ for the fluid should be taken into account. And to accurately model the temperature history of each particle the thermal properties of the fluid, C_p and k , should be temperature dependent since they could differ up to a factor of 10 between different parts of the domain. The convergence problems are mainly due to the fact that the properties of the fluid are calculated from the old temperature. IBOFlow uses a segregated solver, semi implicit method for pressure linked equations consistent (SIMPLEC), which solves the pressure and momentum equations separately and iteratively through use of a velocity correction. To make the solver more robust the energy equation should be included in the SIMPLE iterations so that the fluid properties are updated between iterations, i.e. the velocity field will be based on the new temperature field instead of the old.
- More physical testing is suggested to exactly determine the uncertainty of the various parameters. The reflection parameter could be determined by measuring the amount of powder injected into the plasma and the amount of powder contained on the target. The effect of oxidations would of course provide a measurement uncertainty.
- The post processing tool described in *Section 3.4.1* needs further development to be industrially applicable. It was developed with the aim of being an eye-opener to what can be done to analyze the temperature history and solidification process of the coating. Little time was put into making the software efficient and thus the calculation times are too high. The porosity of the coating is suggested to be added in the future development.

References

- [1] John D. Anderson. *Modern Compressible Flow, With Historical Perspective - Third Edition*. McGraw-Hill, New York, USA, 2003.
- [2] K. Bobzin, E. Lugscheider, R. Nickel, D. Parkot, W. Varava, H. Olivier, and X. Luo. A new concept of the application of shock wave technology in the cold gas dynamic spray process. *Thermal Spray 2007: Global Coating Solutions*, pages 242–247, 2007.
- [3] M. Capitelli, G. Colonna, C. Gorse, and A. D’Angola. Transport properties of high temperature air in local thermodynamic equilibrium. *The European Physics Journal*, D 11:279–289, 2000.
- [4] Yunus A. Çengel and Michael A. Boles. *Thermodynamics, an Engineering Approach. Fourth edition*. McGraw-Hill, New-York, USA, 2002.
- [5] I. Choquet, S. Björklund, J. Johansson, and J. Wigren. Clogging and lump formation during atmospheric plasma spraying with powder injection downstream the plasma gun. *Journal of Thermal Spray Technology*, 16:512–523, 2007.
- [6] Clayton Crowe, Martin Sommerfeld, and Yutaka Tsuji. *Multiphase Flows with Droplets and Particles*. CRC Press LLC, Florida, USA, 1998.
- [7] F. Ben Ettouil, B. Pateyron, H. Ageorges, M. El Ganaoui, P. Fauchais, and O. Mazhorova. Fast modeling of phase changes in a particle injected within a d.c. plasma jet. *Thermal Spray 2007: Global Coating Solutions*, pages 270–275, 2007.
- [8] P. Fauchais, A. Vardelle, and B. Dussoubs. Quo vadis thermal spraying? *Journal of Thermal Spray Thechnology*, 10:44–66, 1999.
- [9] Pierre Fauchais and Armelle Vardelle. Thermal plasmas. *IEEE Transactions on plasma science*, 25:1285–1280, 1997.
- [10] Mingheng Li and Panagiotis D. Christofides. Computational study of particle in-flight behavior in the hvof thermal spray process. *Chemical Engineering Science*, 61:6540–6552, 2006.
- [11] E. Lugscheider, C. Barimani, P. Eckert, and U. Eritt. Modeling of the APS plasma spray process. *Computational Materials Science*, 7:109–114, 1996.
- [12] C. Marchand, C. Chazelas, G. Mariaux, and A. Vardelle. Liquid precursor plasma spraying: Modeling the interactions between the transient plasma jet and the droplets. *Thermal Spray 2007: Global Coating Solutions*, pages 196–201, 2007.
- [13] A. Mark, R. Rundqvist, and F. Edelvik. Comparison between different immersed boundary conditions for simulations of complex fluid flows. *ICMF 2010, Tampa, FL, May 30 - June 4, 2010*, 2010.
- [14] A. Mark and B.G.M. van Wachem. Derivation and validation of a novel implicit second-order accurate immersed boundary method. *Journal of Computational Physics (2008)*, doi:10.1016/j.jcp.2008.03.031.
- [15] Andreas Mark. *The Mirroring Immersed Boundary Method - Modeling Fluids with Moving and Interacting Bodies*. Chalmers University of Technology, Dept. of Applied Mechanics, Div. of Fluid Mechanics, Gothenburg, Sweden, 2008.

- [16] D. Matejka and B. Benko. *Plasma Spraying of Metallic and Ceramic Materials*. John Wiley & Sons Ltd., Chichester, UK, 1989.
- [17] Mathworks. Matlab manual. <http://www.mathworks.com/access/helpdesk/help/techdoc/>, 2008.
- [18] Per Nylén. *The Prediction of Fluid Flow, Particle In-Flight and Coating Characteristics in Atmospheric Plasma Spraying*. Chalmers University of Technology, Dept. of Production Engineering, Gothenburg, Sweden, 1999.
- [19] M. Pasandideh-Fard, S. Chandra, and J. Mostaghimi. A three-dimensional model of droplet impact and solidification. *International Journal of Heat and Mass Transfer*, 45:2229–2242, 2002.
- [20] Lennart Råde and Bertil Westergren. *Mathematics Handbook for Science and Engineering*. Studentlitteratur, Lund, www.studentlitteratur.se, 2004.
- [21] J.P. Trelles, J.V.R. Heberlein, and E. Pfender. Non-equilibrium modelling of arc plasma torches. *Journal of Physics D: Applied Physics*, 40:5937–5952, 2007.
- [22] M. Vardelle, A. Vardelle, P. Fauchais, K.-I. Li, B. Dussoubs, and N. J. Themelis. Controlling particle injection in plasma spraying. *Journal of Thermal Spray Technology*, 10(2):267–284, 2001.
- [23] H K Versteeg and W Malalasekera. *An Introduction to Computational Fluid Dynamics, The Finit Volume Method - Second Edition*. Pearson Education Limited, England, 2007.
- [24] Robert G Watts. *Essentials of Applied Mathematics for Scientists and Engineers*. Morgan & Claypool Publishers, San Rafael, USA, 2007.

Appendix

A Reference Case

Here the specifications of the reference case are given. These settings are used by Volvo Aero when performing the physical testing of the two test cases in *Section 1.4* and the data have been retrieved from Choquet et al. (2007) [5].

Geometry

Nozzle internal diameter	6	mm
Ring external diameter	25	mm
Powder hose length	5	m
Powder injector diameter	1.8	mm
Powder injector offset, jet axis	5	mm
Powder injector offset, radial	6	mm
Powder injector angle	90	°
Spray distance	120	mm

Table A.1: Data from reference case, geometry

Thermal Spray Parameters

Primary gas: argon	40	slpm
Secondary gas: hydrogen	13	slpm
Gun Voltage	63-75	V
Gun Current	600	A
Thermal efficiency	55	%
Carrier gas: argon	4	slpm
Powder	Ni-5wt%Al	
Powder feed rate	54	g/min

Table A.2: Data from reference case, thermal spray parameters

Powder size distribution

Diameter	<45	45-90	90-125	>125
wt%	1.9	96.9	1.2	0

Table A.3: Data from reference case, Powder size distribution

The calculations mentioned in *Section 3.1* are based on the settings given in *Tables A to A*. These data has been retrieved from Choquet (2007) [5] and the aim of the detailed calculations performed in [5] was to predict the backflow of small particles which can lead to clogging and lump formation. The calculations have however proved to be very handy when specifying the setup for the simulations of this work.

B 2D Heat Equation

The transient heat equation in two spatial dimensions is given in *Equation B.1*. Convection is neglected since the aim is to solve the equation in the coating and the substrate, which are assumed to be solid. The equations will be solved assuming separation of variables (Fourier's method) [24, 20].

$$\rho C_p \frac{\partial u}{\partial t} = \frac{\partial}{\partial x} \left(k \frac{\partial u}{\partial x} \right) + \frac{\partial}{\partial y} \left(k \frac{\partial u}{\partial y} \right) \quad (\text{B.1})$$

with boundary conditions

$$u(0, y, t) = u(L, y, t) = u(x, 0, t) = u(x, H, t) = 0 \quad (\text{B.2})$$

and initial condition

$$u(x, y, 0) = T_0 \hat{u}(x, y) \quad (\text{B.3})$$

where $\hat{u}(x, y)$ is an arbitrary function fulfilling the boundary conditions.

Assume that

$$u(x, y, t) = X(x) Y(y) T(t) \quad (\text{B.4})$$

where $X(x)$ is a function of x , $Y(y)$ a function of y , $T(t)$ a function of t . Then *Equation B.1* becomes

$$\frac{1}{\kappa} \frac{T'}{T} = \frac{X''}{X} + \frac{Y''}{Y} \quad (\text{B.5})$$

Since X , Y and T are independent, each term in the right hand side (RHS) must be constant

$$\frac{X''}{X} = A \quad \frac{Y''}{Y} = B \quad (\text{B.6})$$

in *Equation B.5* \rightarrow

$$\frac{T'}{T} = \kappa(A + B) \quad (\text{B.7})$$

Equation B.6 gives the eigenvalue problems [20]

$$X'' - AX = 0 \quad Y'' - BY = 0 \quad (\text{B.8})$$

which have the general solution

$$\begin{aligned} X(x) &= a_1 e^{\sqrt{A}x} + a_2 e^{-\sqrt{A}x} \\ Y(y) &= b_1 e^{\sqrt{B}y} + b_2 e^{-\sqrt{B}y} \end{aligned} \quad (\text{B.9})$$

Equation B.7 has the general solution

$$T(t) = C e^{\kappa(A+B)t} \quad (\text{B.10})$$

Applying the boundary conditions in *Equation B.2* to *Equation B.9* and omitting the trivial solutions $\rightarrow a_1 + a_2 = 0$ and $a_2 e^{-\sqrt{A}L} = -a_1 e^{\sqrt{A}L} \rightarrow$

$$e^{2\sqrt{A}L} = 1$$

Using Euler's formula, $e^{ir} = \cos(r) + i \sin(r)$, with the ansatz $A = (\eta i)^2$ for a real number $\eta \rightarrow$

$$\cos(2\eta L) + i \sin(2\eta L) = 1 \leftrightarrow \eta = \frac{n\pi}{L}$$

\rightarrow

$A = -(\frac{n\pi}{L})^2$ and hence $\sqrt{A} = i\frac{n\pi}{L}$. Analogous for the constant B and using a different version of Euler's formula stated in [20] \rightarrow

$$u(x, y, t) = \sum_{n=1}^{\infty} \sum_{m=1}^{\infty} \beta_{n,m} \sin\left(\frac{n\pi}{L}x\right) \sin\left(\frac{m\pi}{H}y\right) e^{-\kappa((\frac{n\pi}{L})^2 + (\frac{m\pi}{H})^2)t} \quad (\text{B.11})$$

$\beta_{n,m}$ is determined through the initial condition *B.3* \rightarrow

$$\sum_{n=1}^{\infty} \sum_{m=1}^{\infty} \beta_{n,m} \sin\left(\frac{n\pi}{L}x\right) \sin\left(\frac{m\pi}{H}y\right) = \hat{u}(x, y)$$

\rightarrow

$$\beta_{n,m} = \frac{2}{L} \int_0^L \frac{2}{H} \int_0^H \hat{u}(x, y) \sin\left(\frac{n\pi}{L}x\right) \sin\left(\frac{m\pi}{H}y\right) dy dx \quad (\text{B.12})$$

The initial condition is given by a hat function $\hat{u}(x, y) = \varphi(x)\theta(y)$ which linearly increases from 0 on the boundary to 1 in the center as

$$\varphi(x) = \begin{cases} \frac{2x}{L} & x \in [0 \frac{L}{2}[\\ 1 & x = \frac{L}{2} \\ 2(1 - \frac{x}{L}) & x \in]\frac{L}{2} L] \end{cases} \quad \theta(y) = \begin{cases} \frac{2y}{H} & y \in [0 \frac{H}{2}[\\ 1 & y = \frac{H}{2} \\ 2(1 - \frac{y}{H}) & y \in]\frac{H}{2} H] \end{cases} \quad (\text{B.13})$$

Performing the integral calculus on the continuous and piecewise differentiable *Equation B.12* through integration by parts on the intervals $0 < x < \frac{L}{2}$, $\frac{L}{2} < x < L$, $0 < y < \frac{H}{2}$ and $\frac{H}{2} < y < H \rightarrow$

$$\beta_{n,m} = T_0 \frac{64}{n^2 m^2 \pi^4} \sin\left(\frac{n\pi}{2}\right) \sin\left(\frac{m\pi}{2}\right) \quad (\text{B.14})$$

Hence, the analytical solution of the 2D heat equation with Diriclet boundary condition and a hat function initial condition is *Equation B.11* with $\beta_{n,m}$ according to *Equation B.14*.

C Test Case 3

The results of this test did not provide any additional information beyond the two prior test cases. The target plates are seen in *Figures C.1* and *C.2*. The aim of this test was to get a better understanding of the shape of the particle column. As the particles are injected in a 90° angle to the plasma jet this test would visualize the full range from particle injection aligned with the gun movement, to perpendicular to the gun movement. The tests showed that the targets were too small and if, in the future, this test case were to be repeated, it is recommended to use a larger target plate and a wider curve of the gun movement.

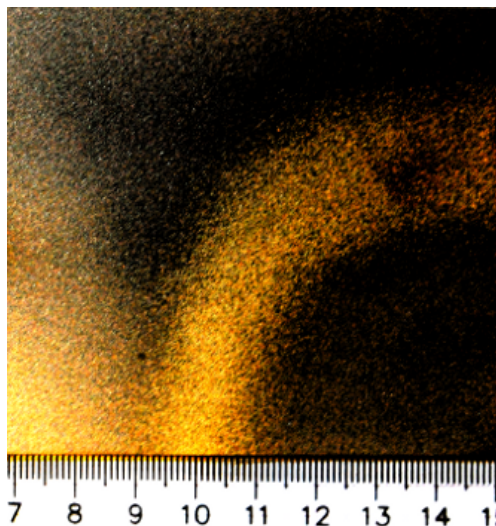


Figure C.1: Test case 3, first target

After spraying the first plate an attempt to capture more of the impacts was made. The gun movement was changed so that the curve would start slightly later but as can be seen in *Figure C.2* the consequence of the change was that only part of the sweep after the bend was captured.

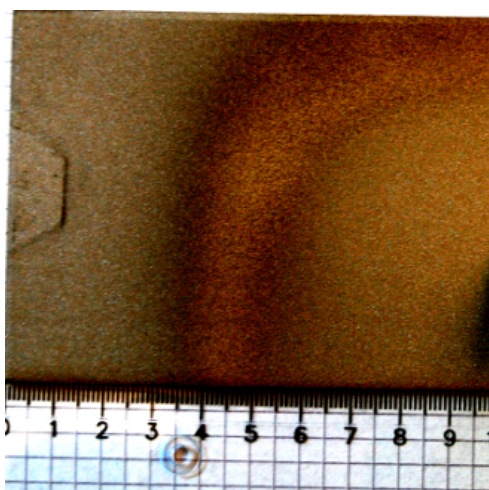


Figure C.2: Test case 3, second target